



Supplement of

Evaluation of transport processes over North China Plain and Yangtze River Delta using MAX-DOAS observations

Yuhang Song et al.

Correspondence to: Cheng Liu (chliu81@ustc.edu.cn)

The copyright of individual parts of the supplement might differ from the article licence.

Section S1. The impacts of stratospheric absorbers.

When SZA is over 75° , the scattering mainly occurs in the lower stratosphere and upper troposphere. At that time, DOAS measurements are very sensitive to stratospheric absorbers, while the sensitivity to near-surface absorbers is relatively lower. In other words, absorbers in stratosphere contribute considerably to the measurements, especially for lower elevation angles during early morning and late evening. In this study, we mainly focused on the tropospheric absorbers close to the ground surface, and thus needed to filter out the measurements with $SZA > 75^\circ$.

Section S2. The impacts of cloud and filtering procedure

In the radiative transfer calculations of the aerosol and trace gas profile retrieval, the layers were assumed to be horizontally homogeneous and cloud impacts were not considered in this calculation process. Notably, the presence of cloud would result in inhomogeneous or/and rapidly fluctuating radiation transport conditions, which might bring uncertainties into the retrieval results. Therefore, we needed to filter the retrieved differential slant column densities (DSCDs) by screening out cloudy scenes before further processing for the profile retrieval (Chan et al., 2019). Since the vertical distribution of the oxygen collision complex O_4 is nearly constant, the retrieved O_4 DSCDs and (relative) intensities ought to vary smoothly with time, or with the solar and viewing geometry. Any rapid change in O_4 DSCDs and intensities suggests a sudden variation of the radiative transport condition, which is possibly linked to the presence of clouds. Thus, to filter data influenced by inhomogeneous and/or rapidly varying radiation transport conditions, we applied a locally weighted regression smoothing filter (LOWESS) (Cleveland, 1981) with a regression window of 3 h to the O_4 DSCDs and intensity time series at each elevation angle. Data with sharp changes in O_4 DSCDs and intensities were filtered out. Only data with slowly varying O_4 DSCDs and intensities were adopted for the subsequent profile retrieval. The limitation of this cloudy scenes removing algorithm is that the algorithm is not able to distinguish between continuous and homogeneous cloud conditions. Nevertheless, it is rare that the cloud does not alter for a long time (within an hour) and the cloud layer keeps homogeneous for all viewing directions.

Section S3. Error calculation and estimation

The smoothing error (\mathbf{S}_s) is a quantification of the error arising from the limited vertical resolution of profile retrieval, which can be calculated by Eq. s1. The noise error (\mathbf{S}_n) represents the fitting error of the DOAS fits, primarily owing to the uncertainty in the measurements. The error of the retrieved state vector ($\hat{\mathbf{S}}$) is considered as the sum of these two independent error sources, $\hat{\mathbf{S}} = \mathbf{S}_s + \mathbf{S}_n$, and can be quantified by Eq. s2 (Frieß et al., 2006). Thus, in this study, we obtained the sum of smoothing and noise errors by averaging the error of retrieved profiles.

$$\mathbf{S}_s = (\mathbf{AK} - 1)\mathbf{S}_a(\mathbf{AK} - 1)^T \quad (\text{s1})$$

$$\hat{\mathbf{S}} = (\mathbf{K}^T \mathbf{S}_\varepsilon^{-1} \mathbf{K} + \mathbf{S}_a^{-1})^{-1} \quad (\text{s2})$$

where \mathbf{AK} is the averaging kernel, which is the sensitivity of the retrieved state to the true state; \mathbf{S}_a and \mathbf{S}_ε are the covariance matrices of a priori and measurement, respectively; \mathbf{K} is the weighting function matrix (Jacobi matrix), describing the sensitivity of the measurement to perturbations in the state vector.

Algorithm error is the discrepancy between the measured (\mathbf{y}) and modelled DSCDs ($F(\mathbf{x}, \mathbf{b})$). As displayed in Eq. s3, the error sources that result in this discrepancy include forward model error from an imperfect approximation of forward function F , forward model parameter error from selection of parameters \mathbf{b} , and errors not related to the forward function parameters, like detector noise (Rogers, 2004). Algorithm error is a function of the viewing angle. Due to the difficulty of assigning this error to each altitude of profile, the algorithm errors on the near-surface values and column densities are usually estimated by calculating the average relative differences between the measured and modeled DSCDs at the minimum and maximum elevation angle (except 90°), respectively (Wagner et al., 2004).

$$\sigma_{\text{algorithm}} = \mathbf{y} - F(\mathbf{x}, \mathbf{b}) \quad (\text{s3})$$

where $F(\mathbf{x}, \mathbf{b})$ is the forward model; \mathbf{b} represents the meteorological parameters; \mathbf{y} is the measured DSCDs; \mathbf{x} is the state vector.

The absorption cross section uncertainty is also an inevitable error source. Assuming the relative error of the cross section is δ , the uncertainty translated into an error in the retrieval space \mathbf{S}_c^x can be calculated in the following operators:

$$\mathbf{S}_c^y = (\delta)^2 \cdot \mathbf{y}\mathbf{y}^T \quad (\text{s4})$$

$$\mathbf{gain} := \frac{\partial \mathbf{x}}{\partial \mathbf{y}} = (\mathbf{K}^T \mathbf{S}_\varepsilon^{-1} \mathbf{K} + \mathbf{S}_a^{-1})^{-1} \mathbf{K}^T \mathbf{S}_\varepsilon \quad (\text{s5})$$

$$\mathbf{S}_c^x = \mathbf{gain} \cdot \mathbf{S}_c^y \cdot \mathbf{gain}^T \quad (\text{s6})$$

where \mathbf{S}_c^y represents the error in the measurement space; the \mathbf{gain} matrix denotes the sensitivity of the state vector \mathbf{x} to measurement \mathbf{y} . Previous study has indicated that the propagated error to the vertical column and vertical profile is similar to the original uncertainty in the cross section (Friedrich et al., 2019). Therefore, we used original cross section uncertainties (O_4 : 4 %, NO_2 : 3 %, and HCHO : 5 %) as our final results.

Owing to a temperature dependence of trace gas absorption, we needed to take into account the error related to the temperature dependence of the cross sections. With two cross sections at two temperatures, we firstly calculate the amplitude changes of the cross sections per Kelvin. Subsequently, we multiply this with the maximum temperature difference (~45K) during the measuring period to estimate this systematic error.

As one of input parameters for trace gas profile retrieval, the aerosol extinction profile plays a crucial role in retrieving the trace gas profile due to its strong impact on the air mass factor (AMF). The errors in the aerosol extinction profile retrieval (e.g., smoothing and noise errors) can be propagate to the trace gas vertical mixing ratio (VMR) and vertical column density

(VCD). To quantify this propagated error, the sensitivity study of the trace gas profile to perturbations in the aerosol extinction profile is demanded. The sensitivity mainly includes slightly increasing the partial aerosol extinction of the i th layer by 1% of the total optical density, and recording the difference between the perturbed and original trace gas profile in the matrix \mathbf{D} . The partial air column information is contained in the diagonal matrix \mathbf{U} . The uncertainty in aerosol profile retrieval is denoted by the matrix $\mathbf{S}_{a,aerosol}$. The errors translated into trace gas VMR profile ($\mathbf{S}_{TG,VMR}^{aerosol}$) can be calculated by Eq. s7, and the errors on the VCD ($\sigma_{TG,VCD}^{aerosol}$) is quantified by Eq. s8:

$$\mathbf{S}_{TG,VMR}^{aerosol} = \mathbf{D}\mathbf{S}_{a,aerosol}\mathbf{D}^T \quad (s7)$$

$$\sigma_{TG,VCD}^{aerosol} = \sqrt{\mathbf{g}^T \mathbf{U} \cdot \mathbf{D} \cdot \mathbf{S}_{a,aerosol} \cdot \mathbf{D}^T \mathbf{U} \cdot \mathbf{g}} \quad (s8)$$

where \mathbf{g} is the total column operator for partial column profiles: $\mathbf{g}^T = (1,1,1,1, \dots, 1)$. In our study, we just roughly estimated the errors of trace gas based on a linear propagation of the errors according to the total error budgets of aerosol retrievals, using Eq. s9:

$$\sigma_{TG}^{aerosol} = \sqrt{(\sigma_{aerosol}^{smooth_noise})^2 + (\sigma_{aerosol}^{algorithm})^2 + (\sigma_{aerosol}^{cross_section})^2 + (\sigma_{aerosol}^{temperature})^2} \quad (s9)$$

where $\sigma_{TG}^{aerosol}$ is the error of trace gas profile caused by aerosol profile retrieval error; $\sigma_{aerosol}^{smooth_noise}$, $\sigma_{aerosol}^{algorithm}$, $\sigma_{aerosol}^{cross_section}$, and $\sigma_{aerosol}^{temperature}$ represent the error budgets of aerosol retrieval related to smoothing and measurement noises, algorithm, cross section, and temperature dependence of cross section, respectively. It is worth noting that algorithm error is not independent of the other error sources, and thus Eq. s9 can only be considered as a rough general estimation of errors related to aerosol retrieval. If a more realistic error estimate is demanded, additional sensitivity tests should be performed for different observation geometries.

Similarly, a general estimation of the total error is based on the square root of the sum of squares of different error terms, using Eq. s10 (for aerosol) or Eq. s11 (for trace gas).

$$\sigma_{total} = \sqrt{(\sigma_{smooth_noise})^2 + (\sigma_{algorithm})^2 + (\sigma_{cross_section})^2 + (\sigma_{temperature})^2} \quad (s10)$$

$$\sigma_{total} = \sqrt{(\sigma_{smooth_noise})^2 + (\sigma_{algorithm})^2 + (\sigma_{cross_section})^2 + (\sigma_{temperature})^2 + (\sigma_{aerosol})^2} \quad (s11)$$

Section S4. Transport flux calculation details, unit conversion and error analysis

Due to the different height grids from the retrieval and the model wind, we needed to design a unified height grid. Thus, we divided 3.1 km into 13 layers: 0–100, 100–200, 200–300, 300–400, 400–600, 600–800, 800–1000, 1000–1200, 1200–1400, 1400–1600, 1600–2000, 2000–3000, 3000–3100 m. We averaged the wind speeds and pollutant concentrations at each layer to represent W_i and C_i in layer i , respectively. In addition, the time resolution of wind simulation is 1 hour, whereas that of the vertical profile is 15 minutes. In order to unify the time resolution, we averaged vertical profiles of an hour to calculate transport flux. Given that the results of last 15 minutes in each hour fit the situation of next hour better, we averaged the

results from -15 min to +45 min as the hourly vertical profiles. For instance, we calculated the average from 9:45 to 10:45 to represent the vertical profile of 10:00.

To better demonstrate transport flux, we needed to convert trace gas mixing ratio (ppb) into molecular density ($\text{molec}\cdot\text{m}^{-3}$) at first. The conversion formula involves temperature and pressure at different altitudes as follows.

$$C = \frac{X \cdot N_A}{V_m} \times 10^{-9} = \frac{X \cdot N_A \cdot P}{R \cdot T} \times 10^{-9} \quad (\text{s12})$$

where C denotes the trace gas molecular density ($\text{molec}\cdot\text{m}^{-3}$), and X is trace gas mixing ratio (ppb); N_A is Avogadro constant ($6.02 \times 10^{23} \text{ mol}^{-1}$); R is molar gas constant, with a value of $8.314 \text{ J}\cdot\text{mol}^{-1}\cdot\text{K}^{-1}$; P and T represent the atmospheric pressure and temperature at different altitudes, respectively. Berberan-Santos et al. (1997) described a relationship model which represents well the dependence of pressure and temperature on altitude for the whole troposphere (below 11 km) as follows.

$$T(z) = T_0 - \beta z \quad (\text{s13})$$

$$P(z) = P(0) \left(1 - \frac{\beta z}{T_0} \frac{mg}{k\beta}\right)^{\frac{mg}{k\beta}} \quad (\text{s14})$$

Here, $T(z)$ and $P(z)$ denote the temperature and atmospheric pressure at height z (km), respectively; T_0 and $P(0)$ are the surface values; k is Boltzmann constant ($1.38 \times 10^{-23} \text{ J}\cdot\text{K}^{-1}$); m is air molecular mass ($29 \times 10^{-3} \text{ kg}\cdot\text{mol}^{-1}$); g represents acceleration of gravity ($9.8 \text{ m}\cdot\text{s}^{-2}$); β equals $6.5 \text{ K}\cdot\text{km}^{-1}$.

Remarkably, there is an error of wind speed (δ_{w_i}) caused by model uncertainty and an error of pollutant concentration (δ_{c_i}) at each layer. These two kinds of errors propagate into the final transport flux results (i.e., F_i and F_c), which can be quantified as follows:

$$\delta_{F_i} = \frac{\partial F_i}{\partial W_i} + \frac{\partial F_i}{\partial C_i} = C_i \times \delta_{w_i} + W_i \times \delta_{C_i} \quad (\text{s15})$$

$$\delta_{F_c} = \sum (\delta_{F_i} \times H_i) = \sum (H_i \times C_i \times \delta_{w_i} + H_i \times W_i \times \delta_{C_i}) \quad (\text{s16})$$

However, an accurate evaluation of wind speed simulation error is an enormous project and involves many factors, such as input parameters, topography and resolution (García-Bustamante et al., 2008; Carvalho et al., 2012; Orrell et al., 2001). By comparing simulation and observation results, Shimada et al. (2011) gave a relationship between relative biases and altitudes. Accordingly, we roughly estimated wind speed relative errors at different heights (0-400 m: 50 %, 400-800 m: 40 %, 800-1200 m: 20 %, 1200-1500 m: 10 %, 1500-3000 m: 3 %, > 3000m: 1 %). For pollutant concentration errors, we mainly considered retrieved errors (i.e., the sum of smoothing and noise errors), which play a dominant role in the total error budgets. The errors of F_i and F_c are displayed in Fig. S6 and Fig. S7, respectively.

Section S5. WRF model and parameter settings

The model adopted in our work is weather research and forecast (WRF) version 4.0. The center of the model domain was set at 102°E, 38°N with a 10 × 10km grid resolution. The 6 hourly final operational global analysis (FNL) data with a 1° × 1° spatial resolution generated by National Centers for Environmental Prediction (NCEP) was utilized as initial and boundary conditions of the simulated weather field. The detailed information of the model configuration options is displayed in Table S2, which can also be found in our previous studies (Liu et al., 2016; Ou et al., 2021).

Section S6. Lagrangian Trajectory Model

The Hybrid Single-particle Lagrangian Integrated Trajectory (HYSPLIT) model is developed by the National Oceanic and Atmospheric Administration Air Resource Laboratory (NOAA-ARL, <http://www.ready.noaa.gov>) (Draxler and Hess, 1998). Several other techniques are often combined with the backward trajectories to further determine the transport pathways and track source origins, such as cluster analysis (CA), potential source contribution function (PSCF), and concentration weighted trajectory (CWT) method, which were utilized in our previous studies (Wang et al., 2020; Hong et al., 2019).

Section S7. The O₄ effective optical path calculation

In order to determine which stations could be contained in the correlation analysis, we needed to calculate the O₄ effective optical path as the distance threshold. The O₄ effective optical path can be calculated as follows (Wagner et al., 2004):

$$L_{O_4} = \frac{DSCD_{O_4}}{n_{O_4}} \quad (s17)$$

where n_{O_4} represents the number density of O₄. The O₄ concentration equals the quadratic O₂ density (Greenblatt et al., 1990), and the O₂ concentration nearly keeps constant, which is proportional to atmospheric density C_{air} . The calculation formula of the O₄ number density is as follows:

$$n_{O_4} = (n_{O_2})^2 = (0.20942 \cdot C_{air})^2 \quad (s18)$$

Atmospheric density C_{air} can be directly calculated using the following formula:

$$C_{air} = \frac{N}{V} = \frac{P \cdot N_A}{T \cdot R} \quad (s19)$$

where N denotes the number of air molecules; V is the volume of air; N_A is Avogadro constant ($6.02 \times 10^{23} \text{ mol}^{-1}$); R is molar gas constant, with a value of $8.314 \text{ J} \cdot \text{mol}^{-1} \cdot \text{K}^{-1}$; P and T represent the atmospheric pressure and temperature, respectively. Here, we used standard atmospheric pressure and temperature, which are $1.01 \times 10^5 \text{ pa}$ and 273.15 K , respectively. After bringing all the values into the formula, we obtained the value of C_{air} , which was $2.69 \times 10^{25} \text{ molec} \cdot \text{m}^{-3}$. Subsequently, we further calculated the n_{O_4} as $3.17 \times 10^{49} \text{ molec}^2 \cdot \text{m}^{-6}$. In this measurement, the average O₄ DCSD was around $1.52 \times 10^{43} \text{ molec}^2 \cdot \text{cm}^{-1}$.

⁵. Accordingly, we could calculate the average O₄ effective optical path in Eq. s17, which was around 4.79 km. Therefore, in this study, we used 5 km as the distance threshold to exclude some stations from the correlation analysis.

Section S8. The abnormal values definition and filtering

For lessening the impacts of “abnormal value” caused by occasional extreme conditions, we needed to adopt a method to seek out the abnormal values and filter them out. In a series of data, we firstly found the first quartile (Q1), median (Q2), and the third quartile (Q3), which are the 25th, 50th and 75th percentile of all values from small to large, respectively. The difference between Q1 and Q3 is called interquartile range (IQR) (i.e., IQR = Q3-Q1). The upper limit (L_{upper}) and lower limit L_{lower} were defined as Q3 plus IQR, and Q1 minus IQR, respectively (i.e., $L_{upper}=Q3+IQR$, $L_{lower}=Q1-IQR$). The values larger than L_{upper} or lower than L_{lower} were defined as abnormal values, and discarded. After filtering the data, the correlation had increased from 0.615 to 0.752, and 0.671 to 0.74, for aerosol and NO₂, respectively.

Section S9. Growth rate calculation

In order to demonstrate the impacts of dust transport on air quality, we needed to select appropriate dates as clean day and dusty day for comparison analysis. Here, clean days were defined as the ones when local surface PM_{2.5} concentrations were less than or equal to 35 ug/m³ (National Ambient Air Quality Standards), while dusty day was the date when the dust storm happened. In addition, to further lessen the effects of other factors (such as climate) and emphasize the role of dust transport, clean days needed to be chosen as close to dust day as possible.

To further quantify the differences between dusty day and clean days, the growth rates of measured pollutants at different heights were introduced to do detailed analysis (Hong et al., 2019). The growth rate was calculated as follows:

$$G = \frac{[p]_{dust} - [p]_{clean}}{[p]_{clean}} \quad (s20)$$

Here, G is the growth rate of the corresponding pollutants, $[p]_{dust}$ and $[p]_{clean}$ represent the average concentration of air pollutants at different heights on dusty day and clean days, respectively.

Section S10. Identification of primary and secondary HCHO in SJZ station

The atmospheric HCHO sources can be classified into primary emissions and secondary formation. The primary sources of HCHO include biogenic sources, such as biomass burning and vegetation (Lee et al., 1997; Andreae, 2019), and anthropogenic activities, such as vehicle emissions, coal combustion and industrial emissions (Carlier et al., 1986; Dong et al., 2014; Liu et al., 2017). The direct HCHO emissions usually accompany incomplete combustion and are closely linked to the emission of CO. Therefore, CO can be used as a tracer for the primary emission of HCHO (Garcia et al., 2006; Friedfeld et al., 2002).

Secondary HCHO can be formed because of the oxidation of volatile organic compounds (VOCs) in the atmosphere (Altshuller, 1993), along with the formation of O₃ (Duan et al., 2008; Levy, 1971). In addition, O₃ reacts with NO emitted from automobiles to form NO₂, and thereby O_x (O_x=O₃+NO₂) has always been considered a tracer for photochemical processes in the urban atmosphere (Wood et al., 2010).

Our study selected CO as the tracer of primary HCHO, with O_x as an indicator of secondary HCHO production. The real-time measured HCHO could be apportioned using a multiple linear regression model, which has been widely utilized in source separation for ambient HCHO (Xue et al., 2022; Su et al., 2019; Garcia et al., 2006; Hong et al., 2018; Friedfeld et al., 2002):

$$[C_{HCHO}] = \beta_0 + \beta_1 \times [C_{CO}] + \beta_2 \times [C_{O_x}] \quad (s21)$$

where β_0 , β_1 , and β_2 are the fitting coefficients obtained from the multiple linear regression, and $[C_{HCHO}]$, $[C_{CO}]$, and $[C_{O_x}]$ represent the concentrations for HCHO, CO, and O_x, respectively. In this study, the concentrations of HCHO and NO₂ were from MAX-DOAS near-surface measurements, while CO and O₃ concentrations were collected from CNEMC. The relative contributions of background concentration, primary emissions, and secondary formation to the total HCHO can be obtained using the following equations:

$$R_{Primary} = \frac{\beta_1 \times [C_{CO}]}{\beta_0 + \beta_1 \times [C_{CO}] + \beta_2 \times [C_{O_x}]} \times 100\% \quad (s22)$$

$$R_{Secondary} = \frac{\beta_2 \times [C_{O_x}]}{\beta_0 + \beta_1 \times [C_{CO}] + \beta_2 \times [C_{O_x}]} \times 100\% \quad (s23)$$

$$R_{Background} = \frac{\beta_0}{\beta_0 + \beta_1 \times [C_{CO}] + \beta_2 \times [C_{O_x}]} \times 100\% \quad (s24)$$

where $R_{Primary}$ represents the contribution from primary sources (vehicle and industrial emissions), $R_{Secondary}$ is the contribution of secondary HCHO (photochemical oxidation), and $R_{Background}$ indicates background contributions to the ambient HCHO, which can neither be accounted as primary nor secondary ones.

In previous studies, the background level of HCHO (β_0) is fixed at 1 ppbv (Su et al., 2019; Hong et al., 2018). Here, we took the slow seasonal variation of background HCHO into account and obtained β_0 through third order Fourier least square fitting, improving the overall correlation between the measured and modeled HCHO from 0.552 to 0.681. The linear regression between the measured and modeled HCHO showed a reasonably good agreement, with a slope of 1.54 and a Pearson correlation coefficient (R) of 0.681 (Fig. S15a).

| MAX-DOAS stations | | | The closest CNEMCs | | Distance (km) | Selected for correlation analysis (True/False) |
|-------------------|-------------------|------------------|--------------------|------------------|------------------|--|
| Codes | Longitude (°E) | Latitude (°N) | Longitude (°E) | Latitude (°N) | | |
| SJZ | 114.61 | 37.91 | 114.64 | 37.90 | 2.86 | True |
| WD | 115.15 | 38.17 | 114.85 | 38.03 | 30.55 | False |
| NC | 116.13 | 39.78 | 116.15 | 39.82 | 4.77 | True |
| CAMS | 116.32 | 39.95 | 116.34 | 39.93 | 2.81 | True |
| XH | 116.98 | 39.76 | 116.72 | 39.56 | 31.50 | False |
| DY | 118.98 | 37.76 | 118.69 | 37.43 | 44.76 | False |
| HNU | 116.81 | 33.98 | 116.80 | 33.98 | 0.92 | True |
| NB | 121.90 | 29.75 | 121.84 | 29.91 | 18.73 | False |

Table S1. The locations of all MAX-DOAS and their corresponding closest China National Environmental Monitoring Centers (CNEMC). In terms of the distance between MAX-DOAS and CNEMC, a total of four stations (bold fonts) were selected for correlation analysis, with stations of distance over 5 km were excluded. We determined 5 km as the distance threshold according to the O₄ effective optical path calculation (Supplementary Sect. S7).

| Option | Parameterization scheme |
|--------------------------|--|
| Microphysics | Lin et al. (Lin et al., 1983) |
| Long-wave radiation | RRTMG (Mlawer et al., 1997) |
| Short-wave radiation | RRTMG (Mlawer et al., 1997) |
| Land-surface | Noah (Ek et al., 2003) |
| Planetary boundary layer | YSU (Mlawer et al., 1997) |
| Cumulus parameterization | Grell-Deveny (Grell and Dévényi, 2002) |

Table S2. Parametric scheme of physical process in WRF model

| Altitude (km) | Clean days | | | | | | | | Dust day | | | |
|------------------|---------------|--------------|--------------|--------------|----------------|--------------|--------------|--------------|----------------|--------------|--------------|--------------|
| | 6 March, 2021 | | | | 22 March, 2021 | | | | 15 March, 2021 | | | |
| | DY | NC | SJZ | XH | DY | NC | SJZ | XH | DY | NC | SJZ | XH |
| 0.0 | 0.382 | 0.378 | 0.326 | 0.245 | 0.638 | 0.483 | 0.368 | 0.364 | 4.483 | 2.257 | 3.073 | 1.166 |
| 0.1 | 0.150 | 0.417 | 0.208 | 0.221 | 0.452 | 0.438 | 0.569 | 0.282 | 4.095 | 1.779 | 2.623 | 1.031 |
| 0.2 | 0.072 | 0.585 | 0.404 | 0.426 | 0.428 | 0.478 | 0.480 | 0.320 | 3.413 | 1.579 | 2.319 | 0.895 |
| 0.3 | 0.078 | 0.697 | 0.557 | 0.598 | 0.434 | 0.498 | 1.116 | 0.393 | 2.666 | 1.332 | 1.949 | 0.755 |
| 0.4 | 0.111 | 0.692 | 0.699 | 0.682 | 0.418 | 0.481 | 0.824 | 0.448 | 2.148 | 1.084 | 1.613 | 0.624 |
| 0.5 | 0.142 | 0.635 | 0.748 | 0.676 | 0.399 | 0.436 | 0.956 | 0.450 | 1.859 | 0.862 | 1.348 | 0.512 |
| 0.6 | 0.164 | 0.551 | 0.733 | 0.606 | 0.373 | 0.381 | 0.918 | 0.421 | 1.602 | 0.674 | 1.123 | 0.418 |
| 0.7 | 0.171 | 0.460 | 0.670 | 0.514 | 0.326 | 0.323 | 0.729 | 0.371 | 1.402 | 0.517 | 0.926 | 0.339 |
| 0.8 | 0.166 | 0.374 | 0.583 | 0.424 | 0.280 | 0.269 | 0.613 | 0.315 | 1.158 | 0.417 | 0.762 | 0.274 |
| 0.9 | 0.168 | 0.340 | 0.560 | 0.393 | 0.261 | 0.242 | 0.683 | 0.293 | 1.004 | 0.363 | 0.676 | 0.231 |
| 1.0 | 0.136 | 0.239 | 0.398 | 0.272 | 0.197 | 0.179 | 0.535 | 0.210 | 0.833 | 0.298 | 0.540 | 0.180 |
| 1.2 | 0.101 | 0.154 | 0.267 | 0.175 | 0.137 | 0.118 | 0.367 | 0.139 | 0.579 | 0.204 | 0.372 | 0.120 |
| 1.4 | 0.089 | 0.120 | 0.225 | 0.138 | 0.116 | 0.091 | 0.304 | 0.111 | 0.431 | 0.151 | 0.287 | 0.085 |
| 1.6 | 0.079 | 0.096 | 0.192 | 0.112 | 0.101 | 0.073 | 0.240 | 0.091 | 0.345 | 0.115 | 0.223 | 0.061 |
| 1.8 | 0.070 | 0.077 | 0.161 | 0.090 | 0.091 | 0.060 | 0.269 | 0.078 | 0.289 | 0.084 | 0.181 | 0.045 |
| 2.0 | 0.061 | 0.063 | 0.141 | 0.074 | 0.084 | 0.050 | 0.315 | 0.067 | 0.241 | 0.063 | 0.159 | 0.035 |
| 2.2 | 0.053 | 0.052 | 0.120 | 0.060 | 0.078 | 0.042 | 0.321 | 0.059 | 0.231 | 0.048 | 0.148 | 0.028 |
| 2.4 | 0.046 | 0.042 | 0.099 | 0.048 | 0.072 | 0.035 | 0.250 | 0.051 | 0.217 | 0.038 | 0.137 | 0.023 |
| 2.6 | 0.038 | 0.034 | 0.084 | 0.038 | 0.065 | 0.029 | 0.234 | 0.044 | 0.165 | 0.032 | 0.123 | 0.019 |
| 2.8 | 0.030 | 0.026 | 0.067 | 0.028 | 0.058 | 0.023 | 0.171 | 0.036 | 0.125 | 0.033 | 0.107 | 0.016 |
| 3.0 | 0.021 | 0.018 | 0.048 | 0.021 | 0.047 | 0.016 | 0.118 | 0.027 | 0.096 | 0.029 | 0.081 | 0.012 |

Table S3. Vertical distribution of aerosol extinction coefficients (AECs) on clean days and dusty day (units: km^{-1}). The bold fonts represent peaks or maximum of vertical profile.

| Altitude (km) | Clean days | | | | | | | | Dust day | | | |
|------------------|---------------|---------------|--------------|--------------|----------------|--------------|--------------|--------------|----------------|--------------|---------------|--------------|
| | 6 March, 2021 | | | | 22 March, 2021 | | | | 15 March, 2021 | | | |
| | DY | NC | SJZ | XH | DY | NC | SJZ | XH | DY | NC | SJZ | XH |
| 0.0 | 0.634 | 10.452 | 5.370 | 7.737 | 3.274 | 4.649 | 6.334 | 4.054 | 11.725 | 2.431 | 18.017 | 2.574 |
| 0.1 | 0.883 | 6.654 | 2.728 | 4.832 | 9.446 | 3.504 | 5.358 | 3.190 | 16.798 | 2.167 | 14.742 | 2.097 |
| 0.2 | 1.016 | 13.869 | 4.942 | 6.823 | 8.509 | 3.890 | 7.079 | 3.663 | 15.587 | 1.888 | 13.011 | 2.081 |
| 0.3 | 1.018 | 17.075 | 7.392 | 8.246 | 6.767 | 4.111 | 7.875 | 4.054 | 13.706 | 1.612 | 11.574 | 1.995 |
| 0.4 | 0.941 | 15.150 | 8.320 | 7.800 | 5.521 | 3.878 | 7.487 | 3.986 | 11.805 | 1.358 | 10.143 | 1.820 |
| 0.5 | 0.829 | 11.681 | 7.601 | 6.499 | 4.665 | 3.377 | 6.468 | 3.594 | 10.046 | 1.133 | 8.742 | 1.601 |
| 0.6 | 0.706 | 8.712 | 6.114 | 5.228 | 4.011 | 2.812 | 5.333 | 3.093 | 8.488 | 0.939 | 7.430 | 1.375 |
| 0.7 | 0.589 | 6.539 | 4.628 | 4.258 | 3.456 | 2.292 | 4.309 | 2.601 | 7.121 | 0.775 | 6.255 | 1.164 |
| 0.8 | 0.485 | 5.007 | 3.434 | 3.552 | 2.967 | 1.852 | 3.452 | 2.164 | 5.955 | 0.639 | 5.232 | 0.975 |
| 0.9 | 0.415 | 3.940 | 2.661 | 2.933 | 2.574 | 1.548 | 2.863 | 1.862 | 5.065 | 0.531 | 4.437 | 0.838 |
| 1.0 | 0.357 | 3.109 | 2.033 | 2.499 | 2.265 | 1.297 | 2.374 | 1.617 | 4.353 | 0.444 | 3.790 | 0.725 |
| 1.2 | 0.264 | 2.023 | 1.185 | 2.079 | 1.799 | 0.910 | 1.626 | 1.236 | 3.275 | 0.311 | 2.798 | 0.548 |
| 1.4 | 0.200 | 1.381 | 0.691 | 1.987 | 1.492 | 0.647 | 1.129 | 0.976 | 2.544 | 0.222 | 2.130 | 0.426 |
| 1.6 | 0.155 | 1.018 | 0.431 | 2.066 | 1.289 | 0.471 | 0.817 | 0.799 | 2.041 | 0.162 | 1.678 | 0.341 |
| 1.8 | 0.123 | 0.816 | 0.315 | 2.221 | 1.152 | 0.355 | 0.617 | 0.676 | 1.730 | 0.122 | 1.368 | 0.282 |
| 2.0 | 0.102 | 0.724 | 0.290 | 2.407 | 1.062 | 0.279 | 0.506 | 0.595 | 1.554 | 0.095 | 1.157 | 0.240 |
| 2.2 | 0.087 | 0.708 | 0.316 | 2.608 | 0.999 | 0.228 | 0.469 | 0.542 | 1.497 | 0.077 | 1.011 | 0.211 |
| 2.4 | 0.076 | 0.740 | 0.371 | 2.816 | 0.962 | 0.197 | 0.481 | 0.513 | 1.487 | 0.065 | 0.913 | 0.192 |
| 2.6 | 0.070 | 0.787 | 0.444 | 3.054 | 0.964 | 0.181 | 0.531 | 0.502 | 1.539 | 0.058 | 0.851 | 0.180 |
| 2.8 | 0.067 | 0.880 | 0.531 | 3.342 | 0.983 | 0.176 | 0.631 | 0.506 | 1.649 | 0.054 | 0.823 | 0.174 |
| 3.0 | 0.068 | 1.006 | 0.633 | 3.718 | 1.031 | 0.179 | 0.750 | 0.530 | 1.825 | 0.053 | 0.836 | 0.176 |

Table S4. Vertical distribution of NO₂ on clean days and dusty day (units: ppb). The bold fonts represent peaks or maximum of vertical profile.

| Altitude (km) | Clean days | | | | | | | | Dust day | | | |
|------------------|---------------|--------------|--------------|--------------|----------------|--------------|--------------|--------------|----------------|----|--------------|----|
| | 6 March, 2021 | | | | 22 March, 2021 | | | | 15 March, 2021 | | | |
| | DY | NC | SJZ | XH | DY | NC | SJZ | XH | DY | NC | SJZ | XH |
| 0.0 | 0.622 | 1.008 | 0.829 | 0.921 | 0.836 | 1.024 | 0.996 | 1.011 | 5.022 | | 4.771 | |
| 0.1 | 0.638 | 1.196 | 0.947 | 0.894 | 1.043 | 1.057 | 1.037 | 0.980 | 5.323 | | 4.251 | |
| 0.2 | 0.650 | 1.423 | 1.082 | 0.959 | 1.168 | 1.147 | 1.152 | 0.988 | 5.210 | | 3.794 | |
| 0.3 | 0.644 | 1.581 | 1.153 | 1.037 | 1.207 | 1.207 | 1.265 | 0.998 | 4.918 | | 3.400 | |
| 0.4 | 0.624 | 1.647 | 1.172 | 1.087 | 1.185 | 1.218 | 1.344 | 0.997 | 4.548 | | 3.056 | |
| 0.5 | 0.593 | 1.637 | 1.144 | 1.097 | 1.127 | 1.189 | 1.381 | 0.976 | 4.161 | | 2.754 | |
| 0.6 | 0.554 | 1.573 | 1.084 | 1.073 | 1.049 | 1.131 | 1.376 | 0.931 | 3.785 | | 2.485 | |
| 0.7 | 0.512 | 1.478 | 1.005 | 1.024 | 0.963 | 1.056 | 1.338 | 0.869 | 3.432 | | 2.245 | |
| 0.8 | 0.469 | 1.367 | 0.918 | 0.959 | 0.876 | 0.974 | 1.275 | 0.799 | 3.105 | | 2.029 | |
| 0.9 | 0.427 | 1.252 | 0.832 | 0.887 | 0.792 | 0.891 | 1.198 | 0.727 | 2.807 | | 1.835 | |
| 1.0 | 0.388 | 1.138 | 0.751 | 0.814 | 0.714 | 0.810 | 1.113 | 0.658 | 2.536 | | 1.660 | |
| 1.2 | 0.316 | 0.919 | 0.601 | 0.663 | 0.572 | 0.656 | 0.924 | 0.530 | 2.065 | | 1.360 | |
| 1.4 | 0.256 | 0.737 | 0.480 | 0.535 | 0.458 | 0.528 | 0.754 | 0.426 | 1.683 | | 1.115 | |
| 1.6 | 0.208 | 0.592 | 0.385 | 0.430 | 0.368 | 0.425 | 0.612 | 0.342 | 1.372 | | 0.913 | |
| 1.8 | 0.173 | 0.491 | 0.316 | 0.359 | 0.302 | 0.352 | 0.520 | 0.281 | 1.128 | | 0.747 | |
| 2.0 | 0.144 | 0.410 | 0.261 | 0.301 | 0.248 | 0.293 | 0.445 | 0.231 | 0.930 | | 0.610 | |
| 2.2 | 0.121 | 0.344 | 0.216 | 0.253 | 0.203 | 0.245 | 0.384 | 0.191 | 0.767 | | 0.498 | |
| 2.4 | 0.102 | 0.291 | 0.179 | 0.215 | 0.168 | 0.205 | 0.335 | 0.157 | 0.635 | | 0.406 | |
| 2.6 | 0.088 | 0.248 | 0.150 | 0.184 | 0.138 | 0.174 | 0.296 | 0.130 | 0.529 | | 0.331 | |
| 2.8 | 0.076 | 0.215 | 0.126 | 0.160 | 0.115 | 0.149 | 0.267 | 0.108 | 0.442 | | 0.270 | |
| 3.0 | 0.068 | 0.189 | 0.108 | 0.142 | 0.096 | 0.129 | 0.247 | 0.091 | 0.374 | | 0.219 | |

Table S5. Vertical distribution of HCHO on clean days and dusty day (units: ppb). The bold fonts represent peaks or maximum of vertical profile.

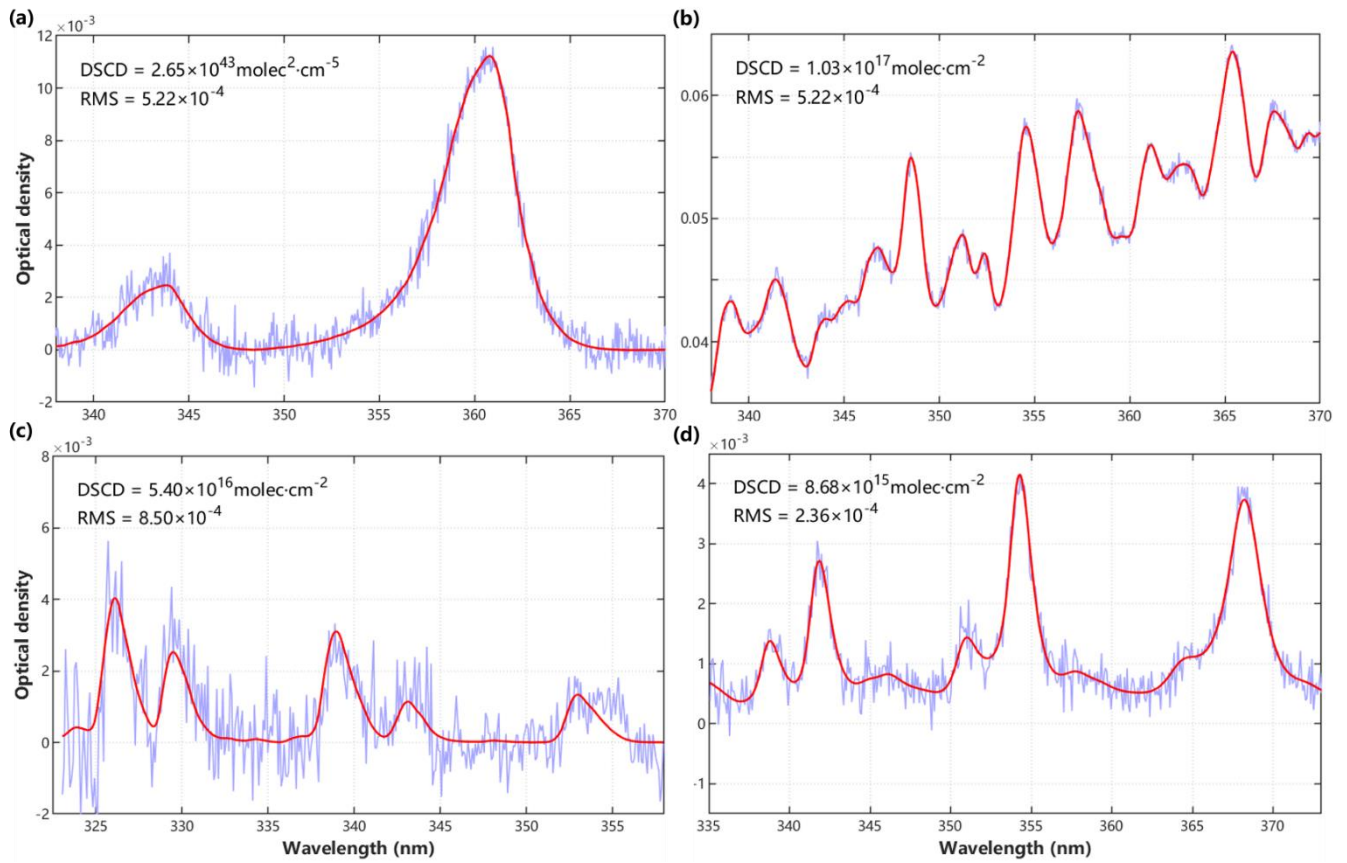


Fig. S1. Typical DOAS spectral fittings for (a) O_4 , (b) NO_2 , (c) $HCHO$, and (d) $HONO$. The detection limit: O_4 : 2.4×10^{42} $molec^2 \cdot cm^{-5}$, NO_2 : 1.7×10^{15} $molec \cdot cm^{-2}$, $HCHO$: 8.9×10^{15} $molec \cdot cm^{-2}$, and $HONO$: 2.5×10^{15} $molec \cdot cm^{-2}$.

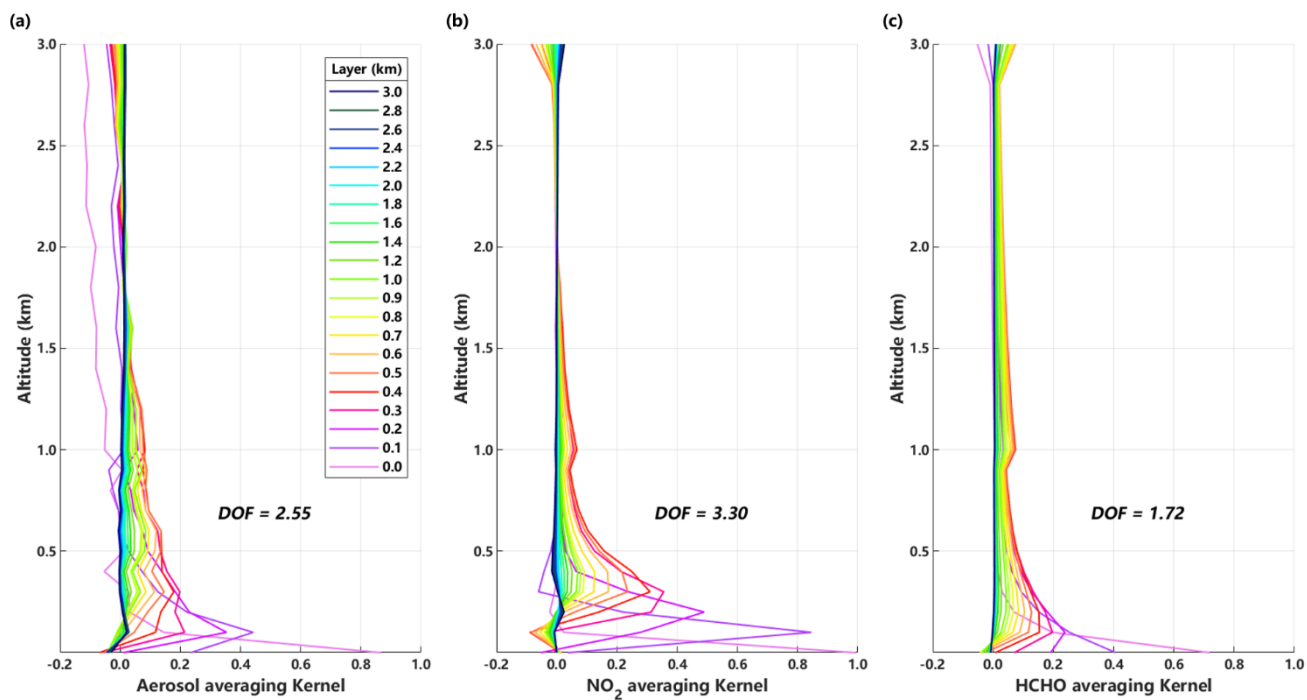


Fig. S2. An example of averaging kernel results from MAX-DOAS measurements at HNU station (March 6, 2021 at 14:33 LT) for (a) aerosol extinction, (b) NO_2 , and (c) HCHO.

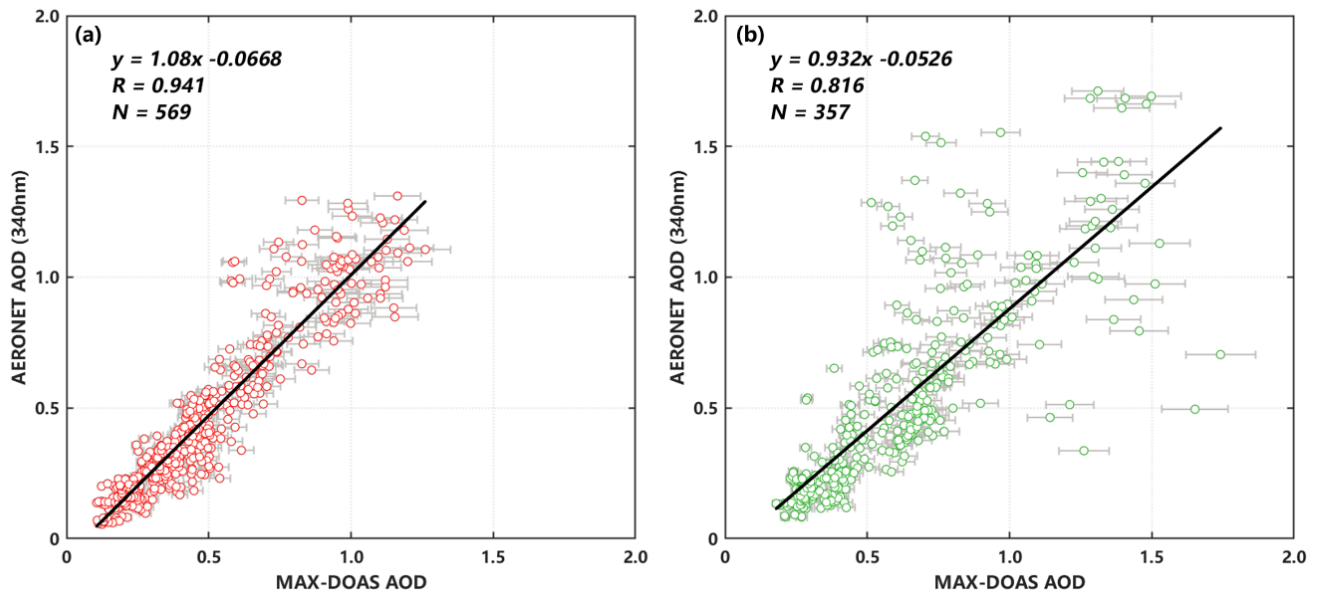


Fig. S3. Correlation analysis of 15-min averaged AOD from AERONET and MAX-DOAS at (a) CAMS, and (b) XH stations from January to March, 2021.

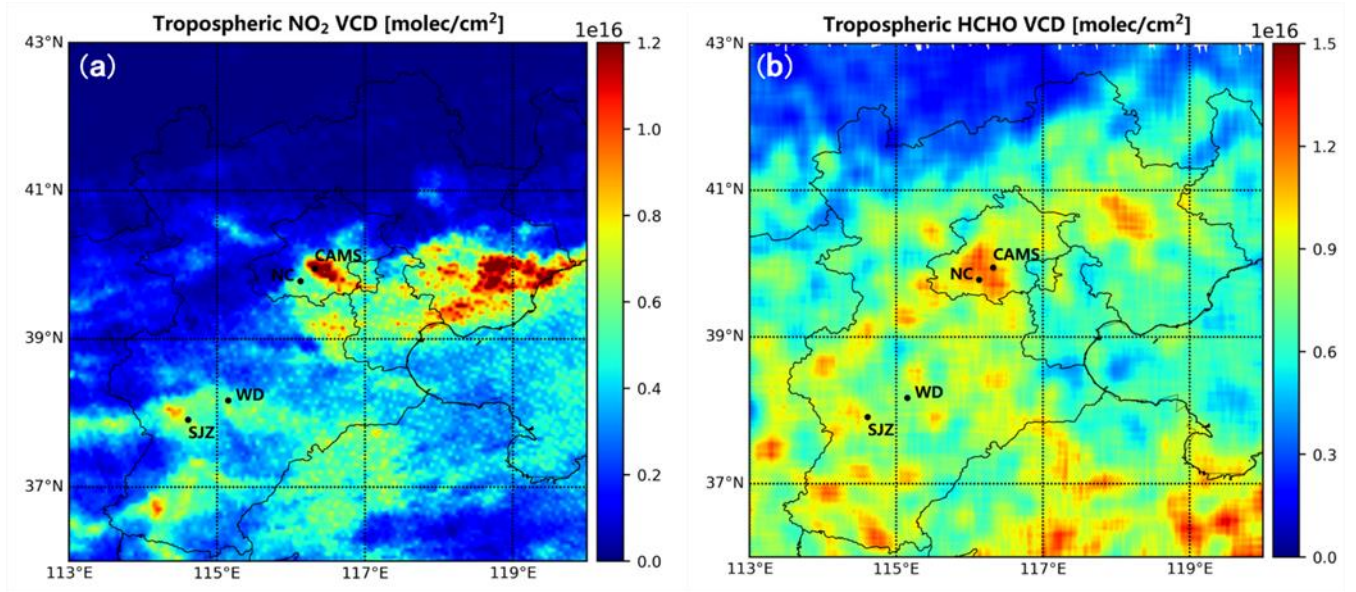


Fig. S4. The spatial distribution of (a) NO₂ and (b) HCHO in the JJJ region measured by TROPOMI on February 5, 2021.

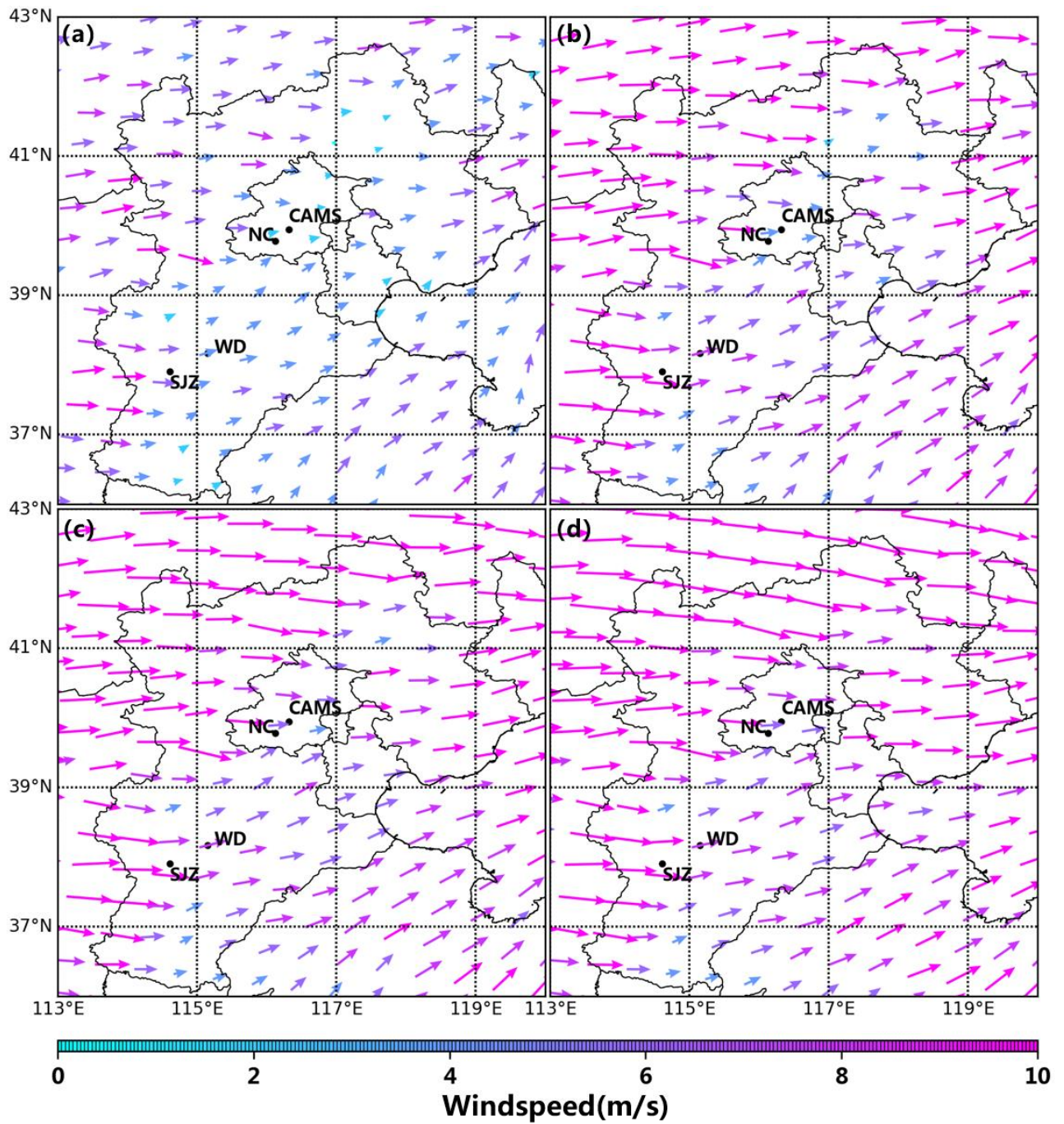


Fig. S5. The wind field in the (a) 0–20, (b) 200–400, (c) 400–600, and (d) 600–800 m layers simulated by WRF at 13:30 on February 5, 2021. The arrows represent the wind direction, and their lengths and colours stand for the wind speed.

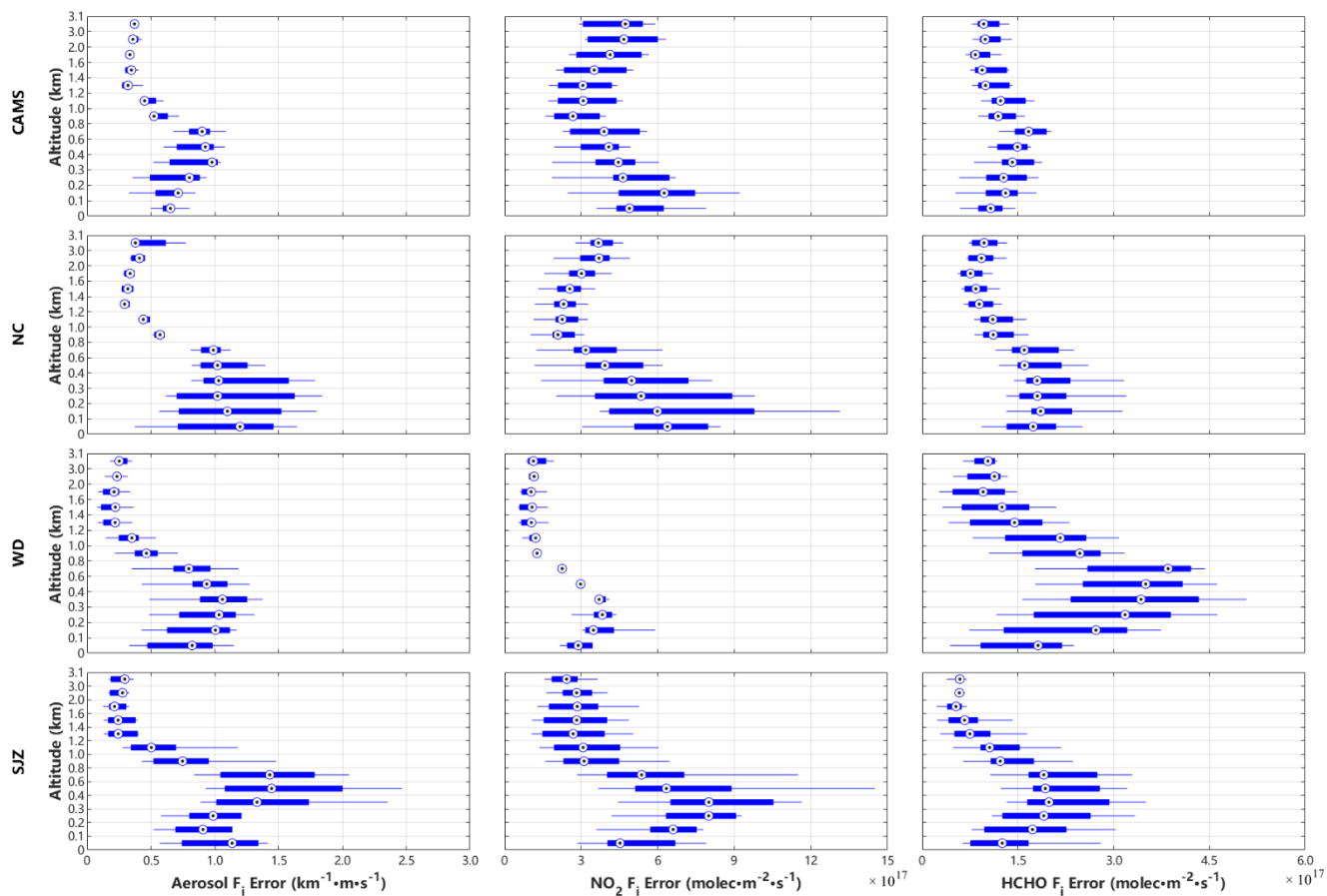


Fig. S6. The vertical distribution of F_i errors at SJZ, WD, NC, and CAMS stations for AECs, NO_2 , and HCHO.

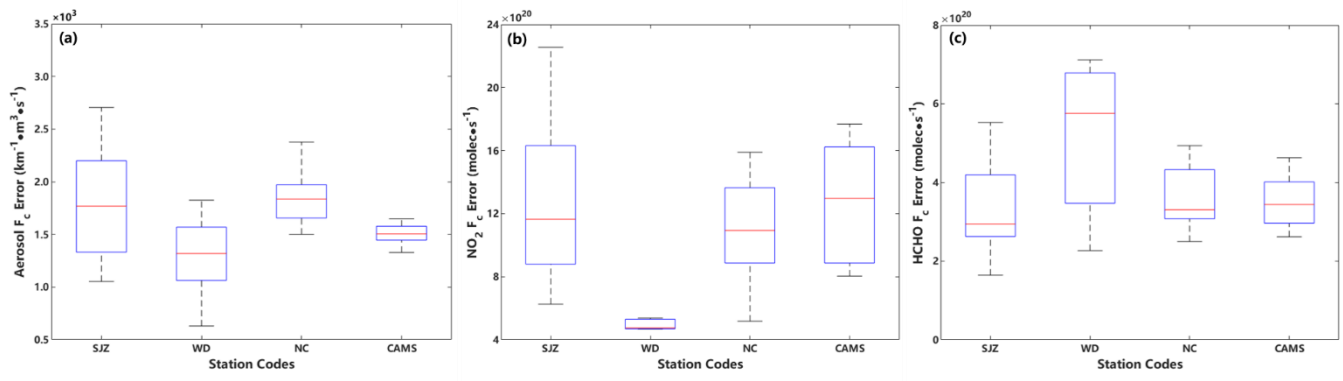


Fig. S7. The F_c errors at SJZ, WD, NC, and CAMS stations for (a) AECs, (b) NO_2 , and (c) HCHO.

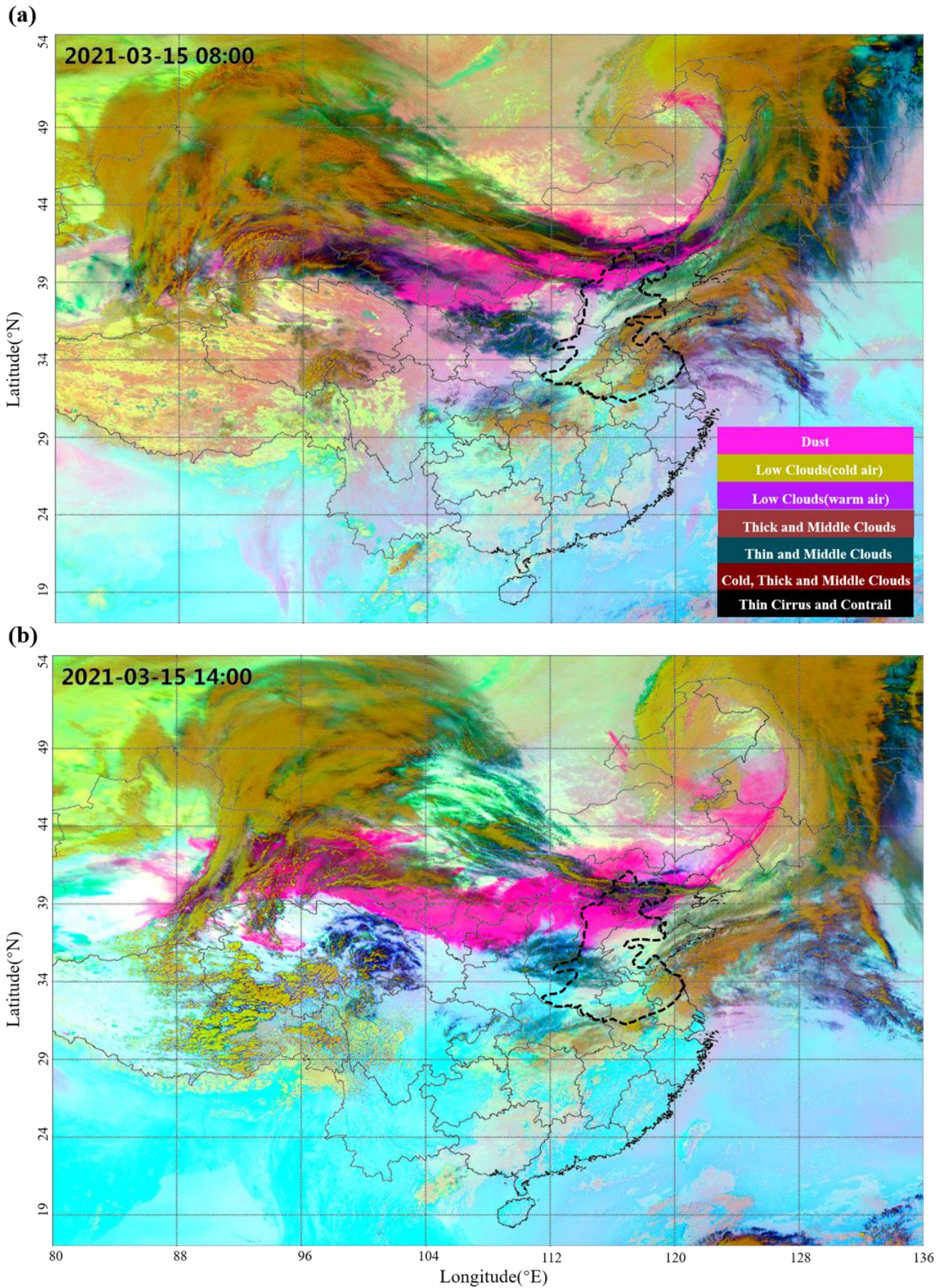


Fig. S8. The Himawari-8 observations: a severe dust storm invaded northern China at (a) 8:00 and (b) 14:00 on March 15, 2021. The dashed black contour line indicates the NCP region.

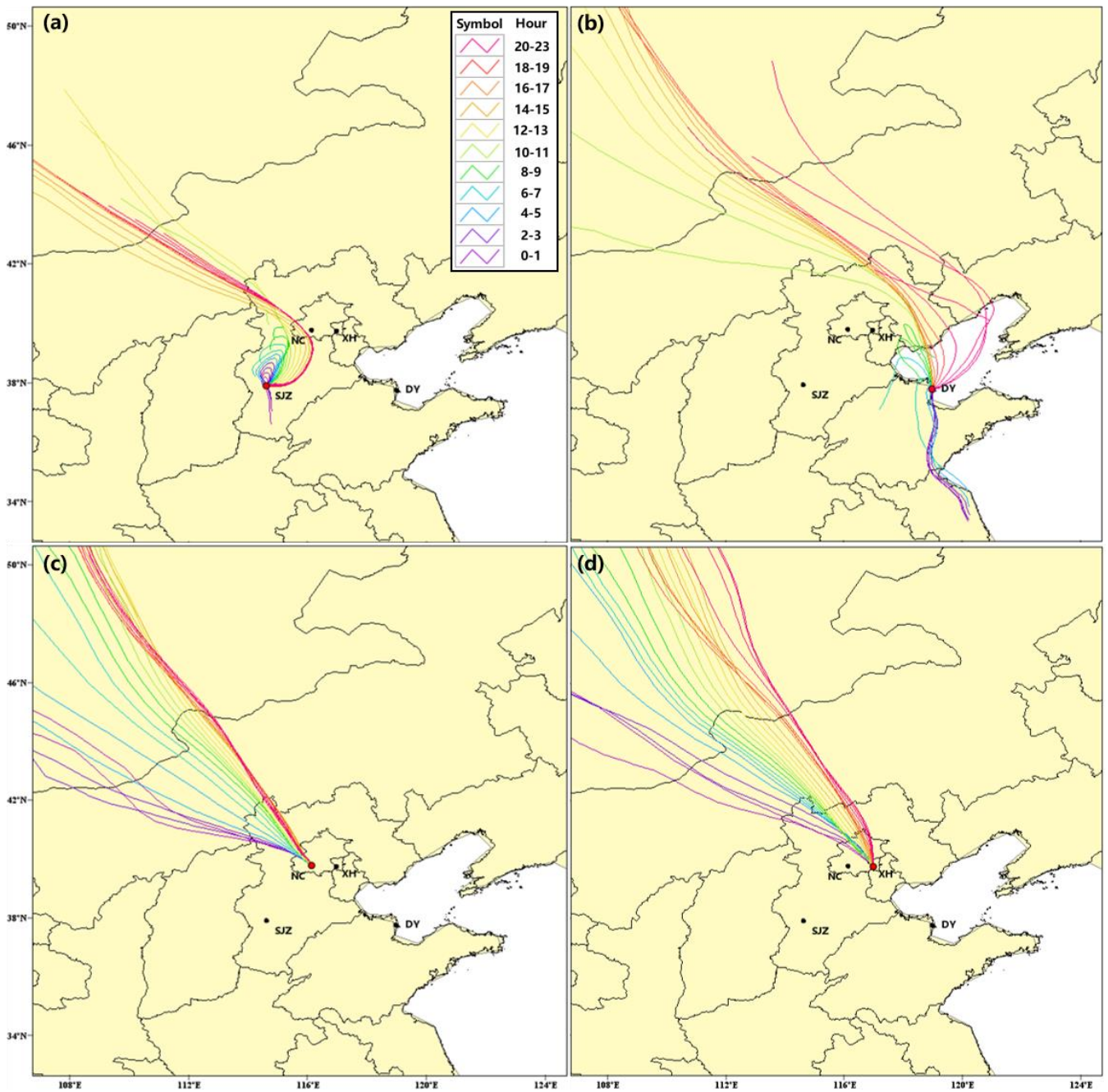


Fig. S9. The 24-h backward trajectory results of (a) SJZ, (b) DY, (c) NC, and (d) XH from 00:00 to 23:00 on March 15, 2021 by means of the HYSPLIT model. The altitude of the receptor site was set to the 100 m above ground level.

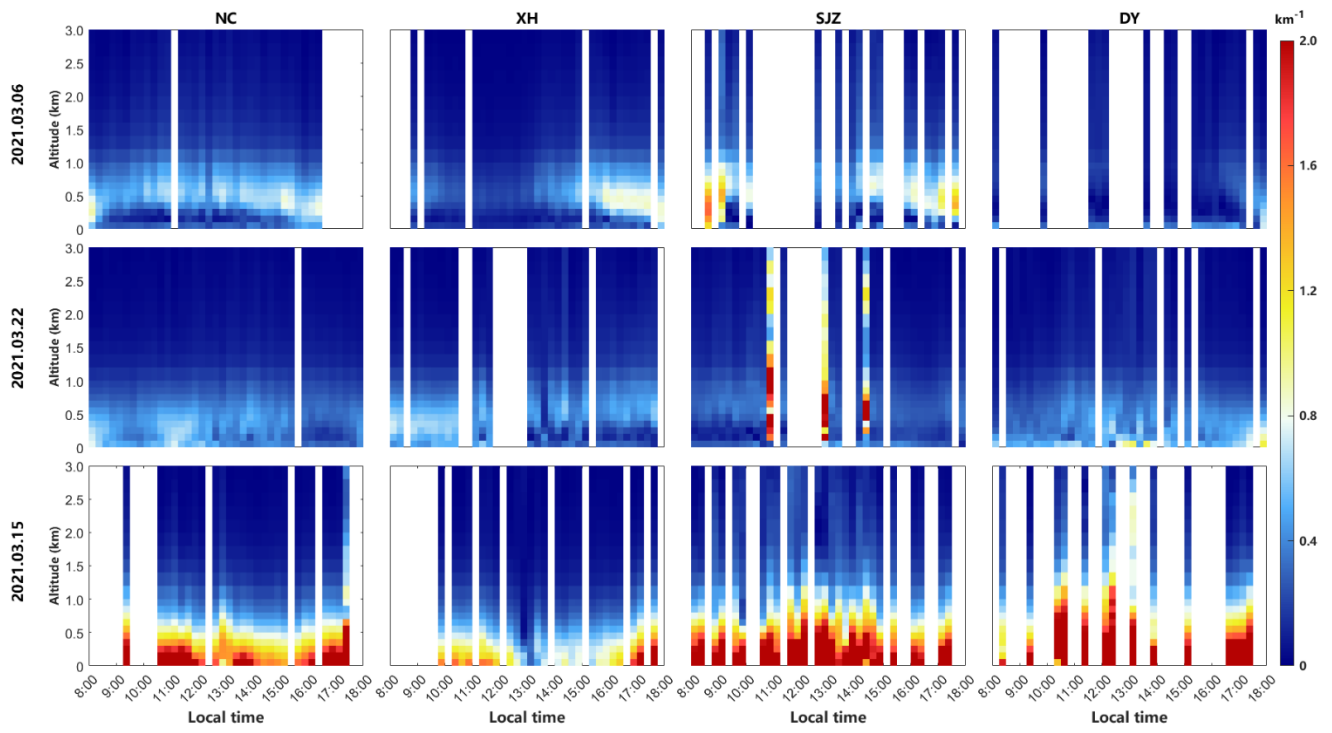


Fig. S10. Vertical profiles of AEC at NC, XH, SJZ, and DY stations during clean days (March 6 and 22, 2021) and dusty day (March 15, 2021). The first line represented the results of March 6, the second and the third corresponded to March 22 and 15, respectively.

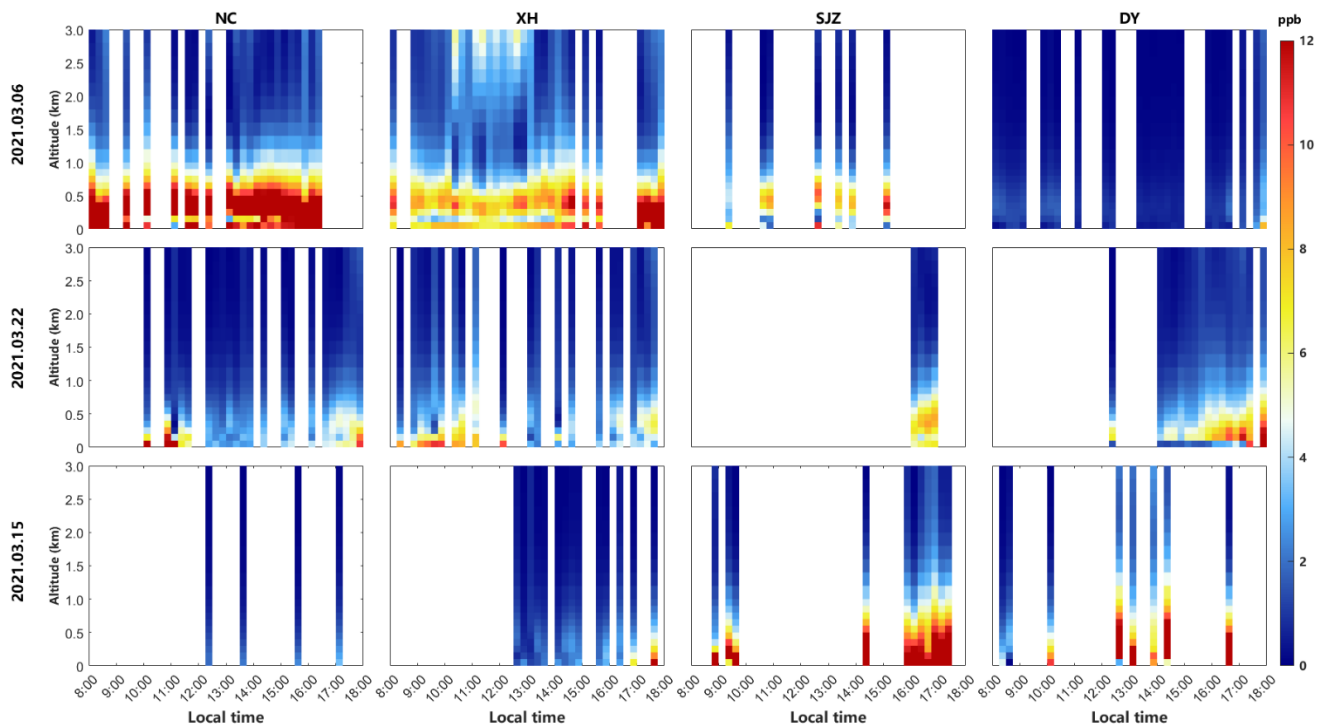


Fig. S11. Vertical profiles of NO_2 at NC, XH, SJZ, and DY stations during clean days (March 6 and 22, 2021) and dust day (March 15, 2021). The first line represented the results of March 6, the second and the third corresponded to March 22 and 15, respectively.

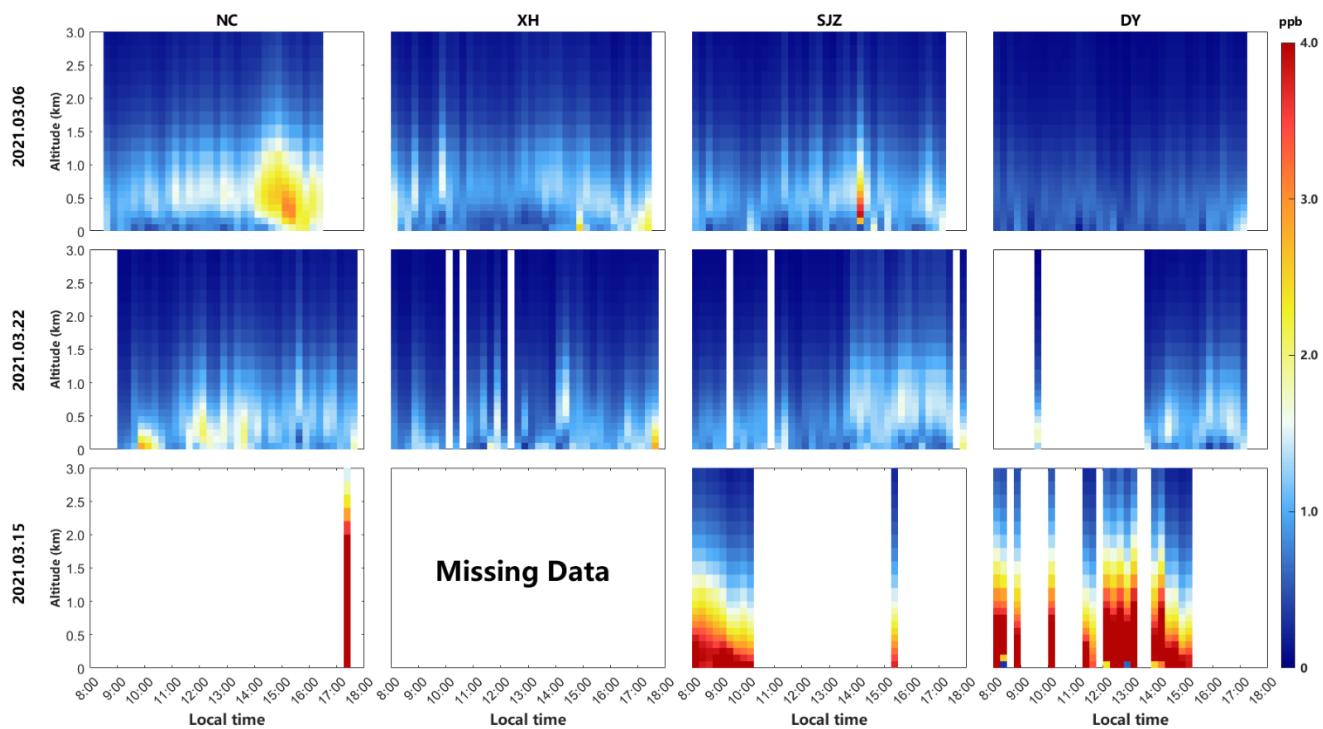


Fig. S12. Vertical profiles of **HCHO** at NC, XH, SJZ, and DY stations during clean days (March 6 and 22, 2021) and dust day (March 15, 2021). The first line represented the results of March 6, the second and the third corresponded to March 22 and 15, respectively.

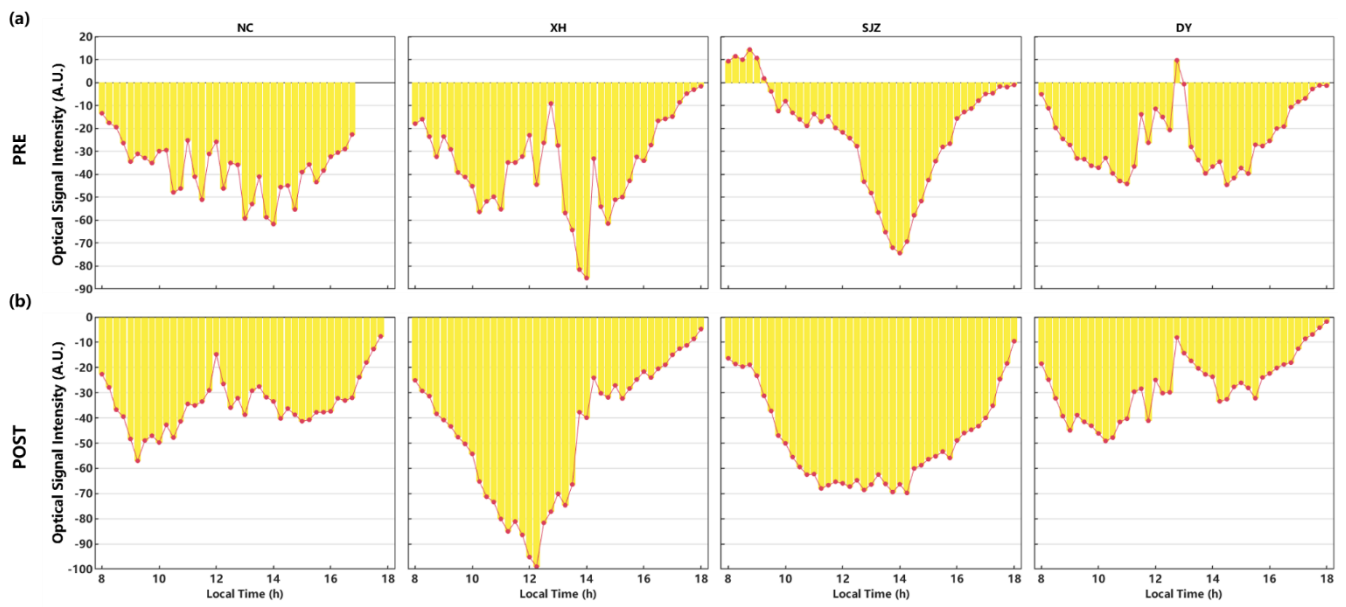


Fig. S13. The difference of optical signal intensities received by MAX-DOAS between dusty day and clean days. (a) PRE: Intensity (March, 15) – Intensity (March, 6); (b) POST: Intensity (March, 15) – Intensity (March, 22).

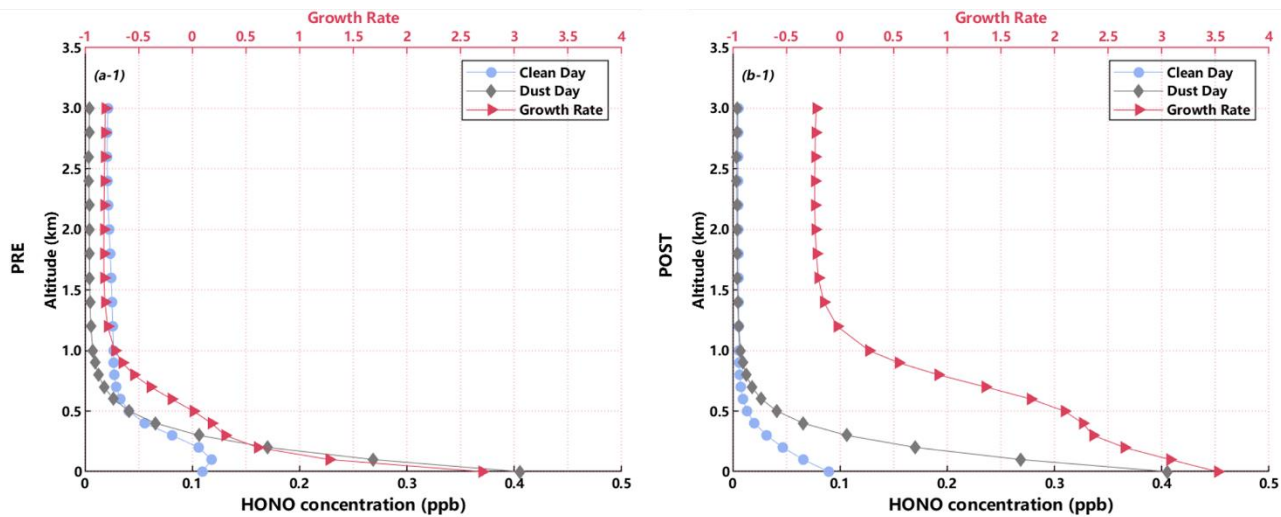


Fig. S14. The growth rates of HONO at different altitudes at NC station. (a-1) PRE: precomparison results between March 6 and 15, 2021, with March 6, 2021 as clean day. (b-1) POST: postcomparison results between March 22 and 15, 2021, with March 22, 2021 as clean day.

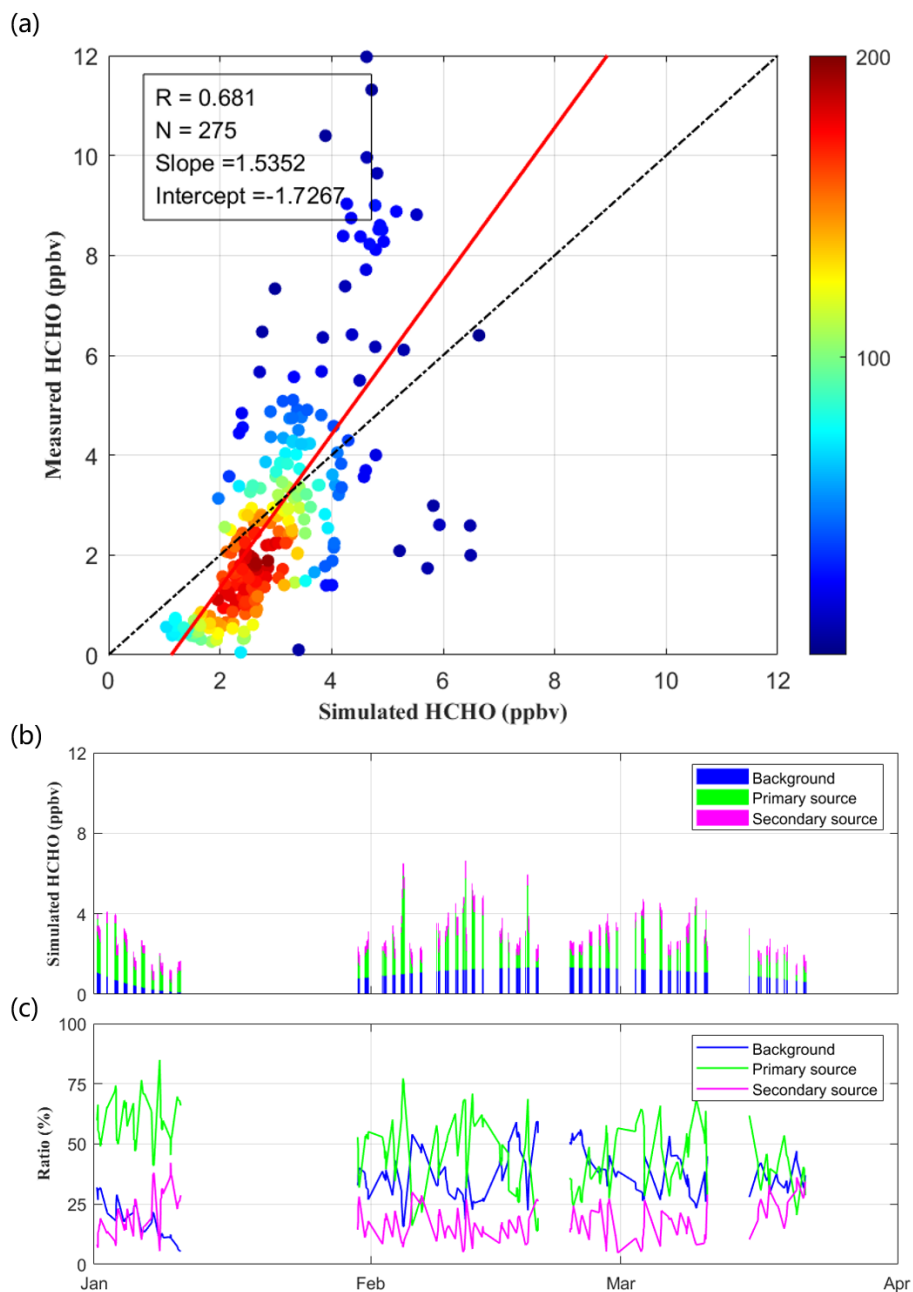


Fig. S15. (a) Comparison analysis of the three-month measured and simulated HCHO values from multiple linear regression from January to March, 2021 at SJZ. Time series of (b) absolute and (c) relative contribution of the primary source, secondary source and atmospheric background to ambient HCHO levels from January to March.

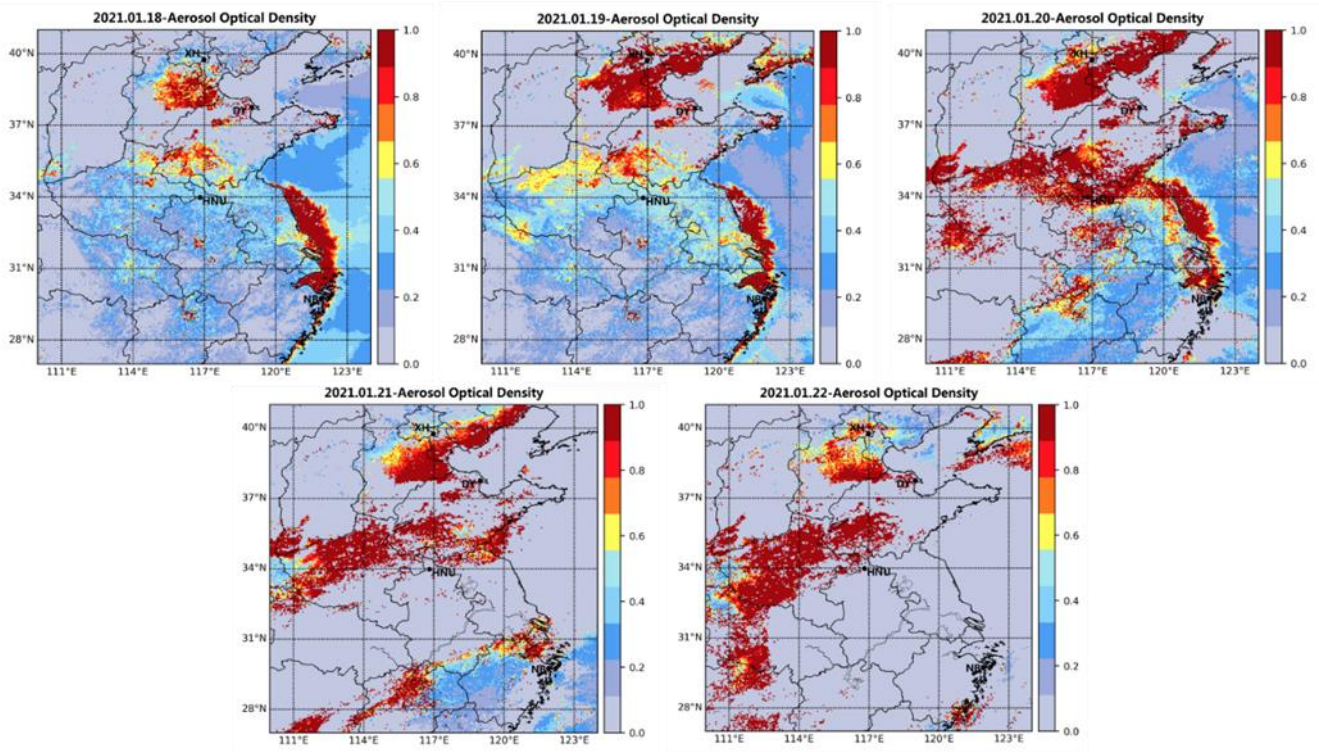


Fig. S16. The spatial distribution of AOD measured by Himawari-8 on January 18-22, 2021.

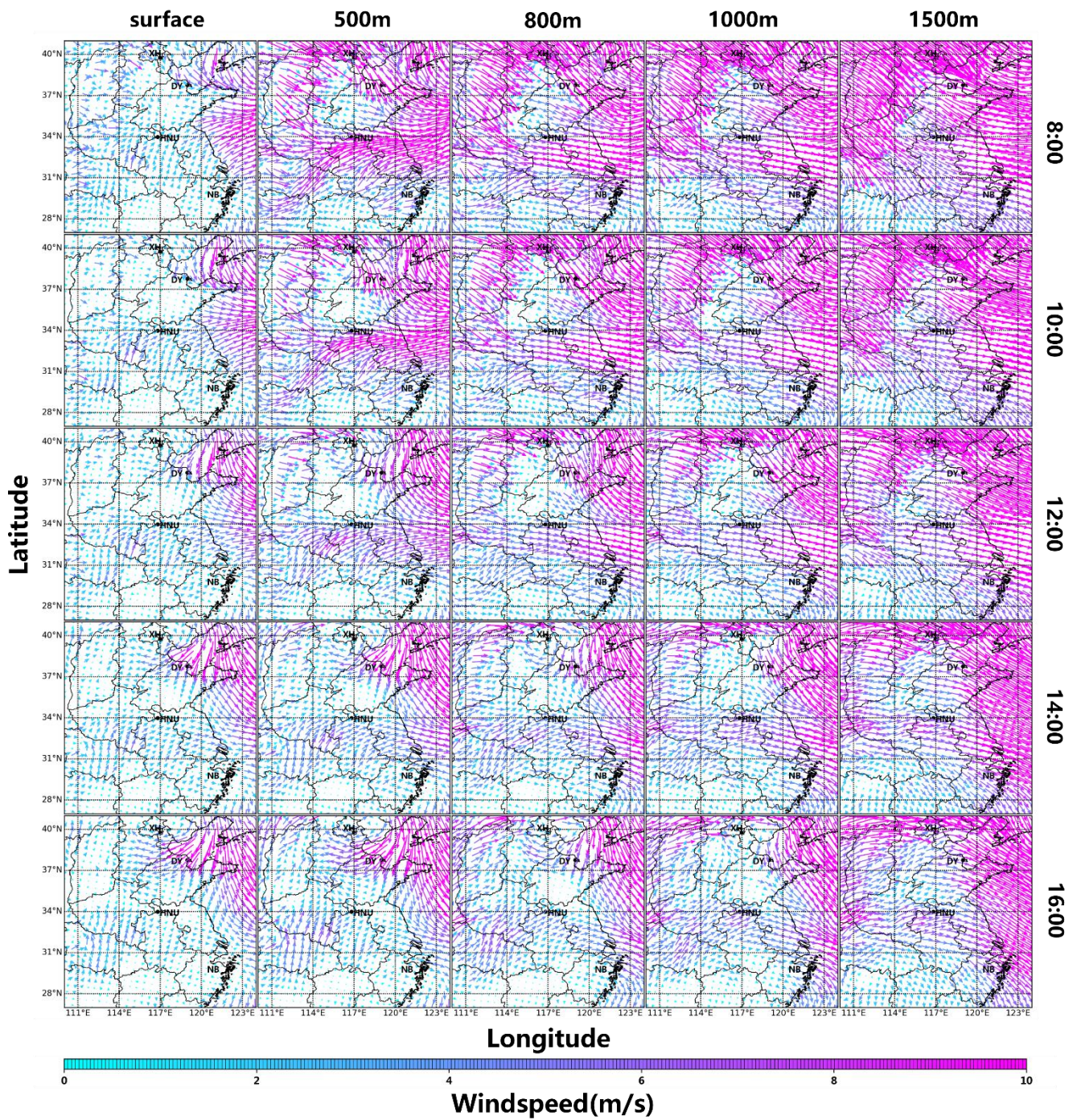


Fig. S17. The diurnal variation in wind fields in layers of surface, 500, 800, 1000 and 1500 m on **January 18, 2021**, respectively. The arrows represent the wind direction, and their lengths and colours stand for the wind speed.

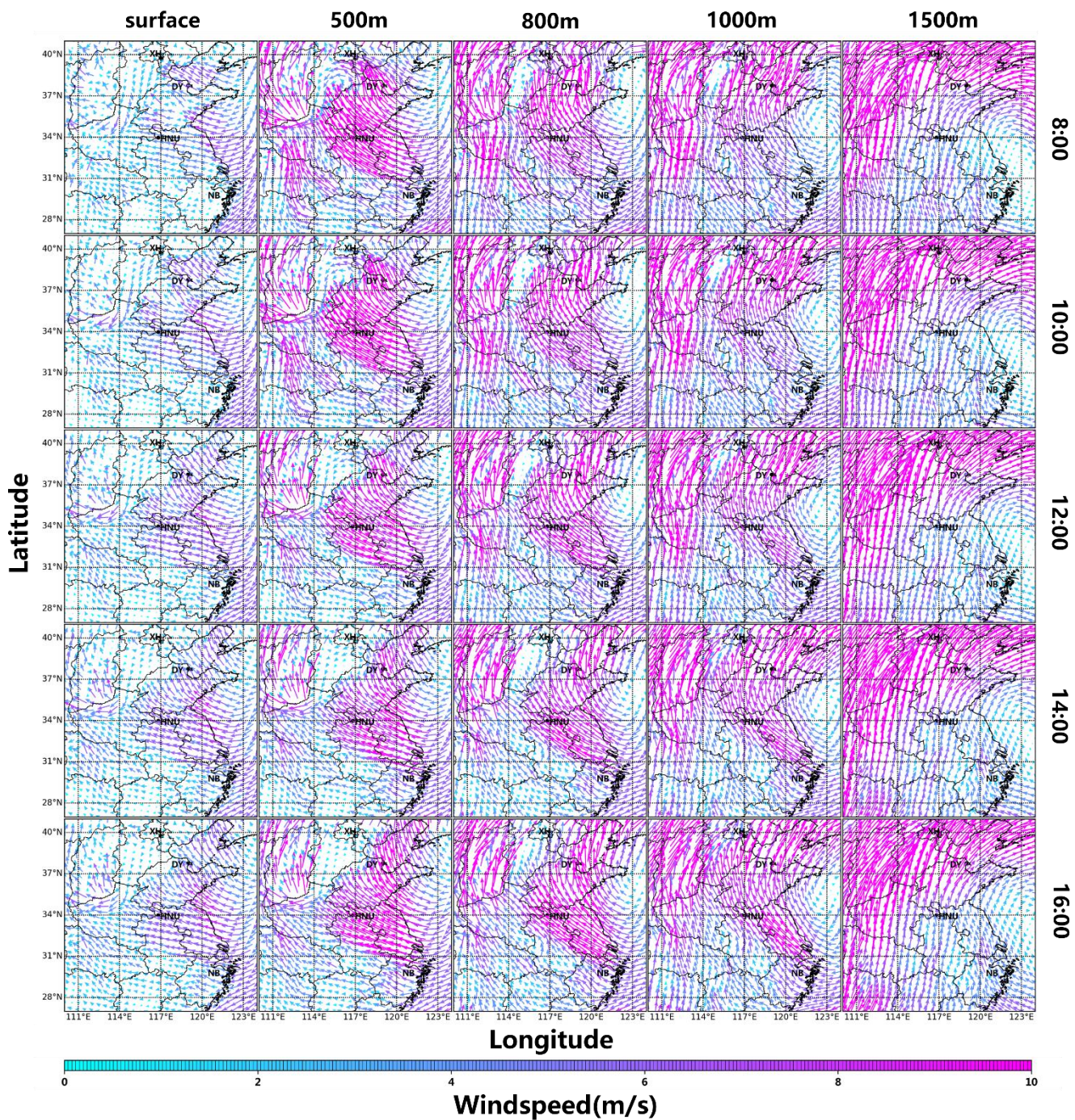


Fig. S18. The diurnal variation in wind fields in layers of surface, 500, 800, 1000 and 1500 m on **January 19, 2021**, respectively. The arrows represent the wind direction, and their lengths and colours stand for the wind speed.

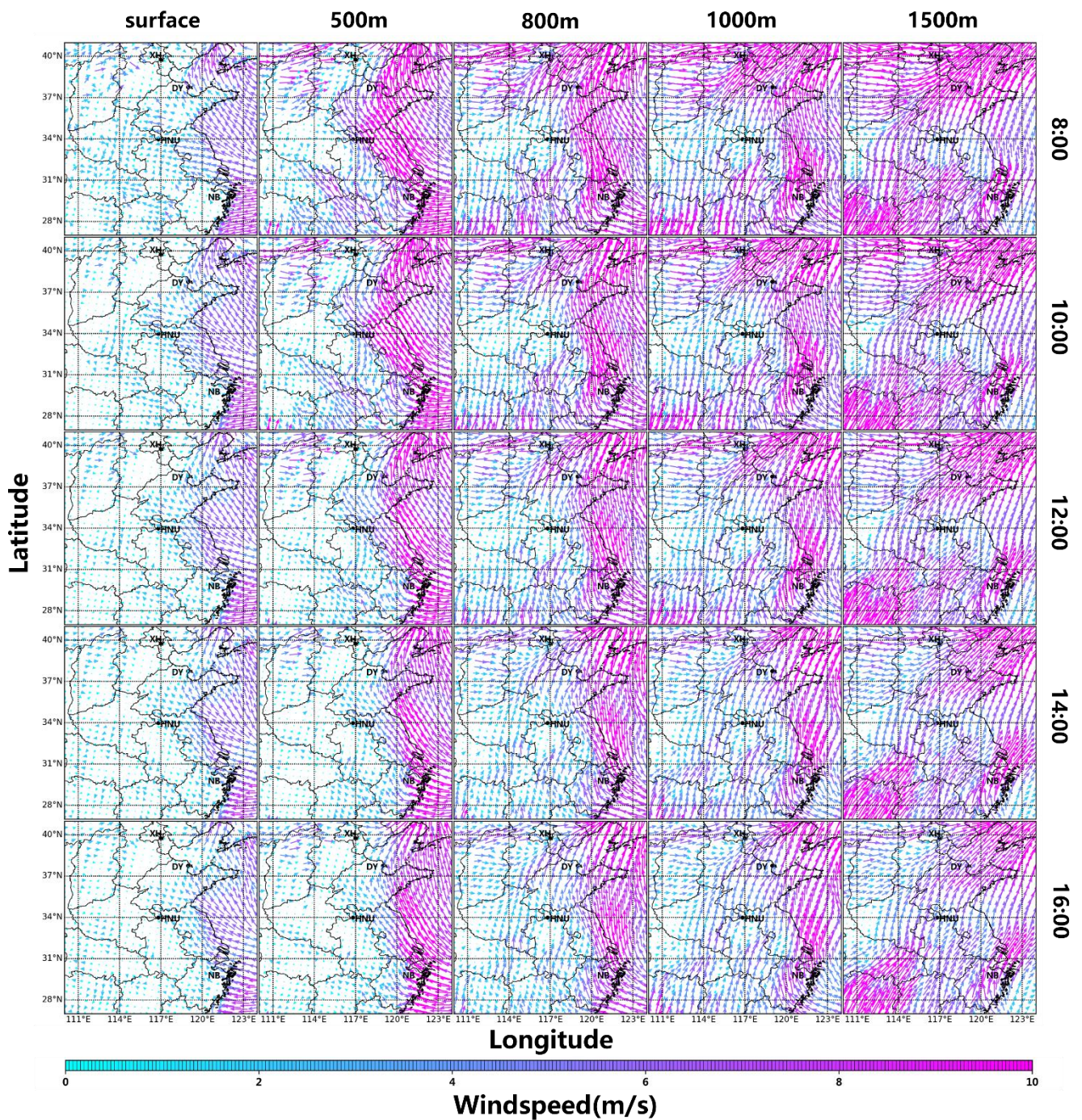


Fig. S19. The diurnal variation in wind fields in layers of surface, 500, 800, 1000 and 1500 m on **January 20, 2021**, respectively. The arrows represent the wind direction, and their lengths and colours stand for the wind speed.

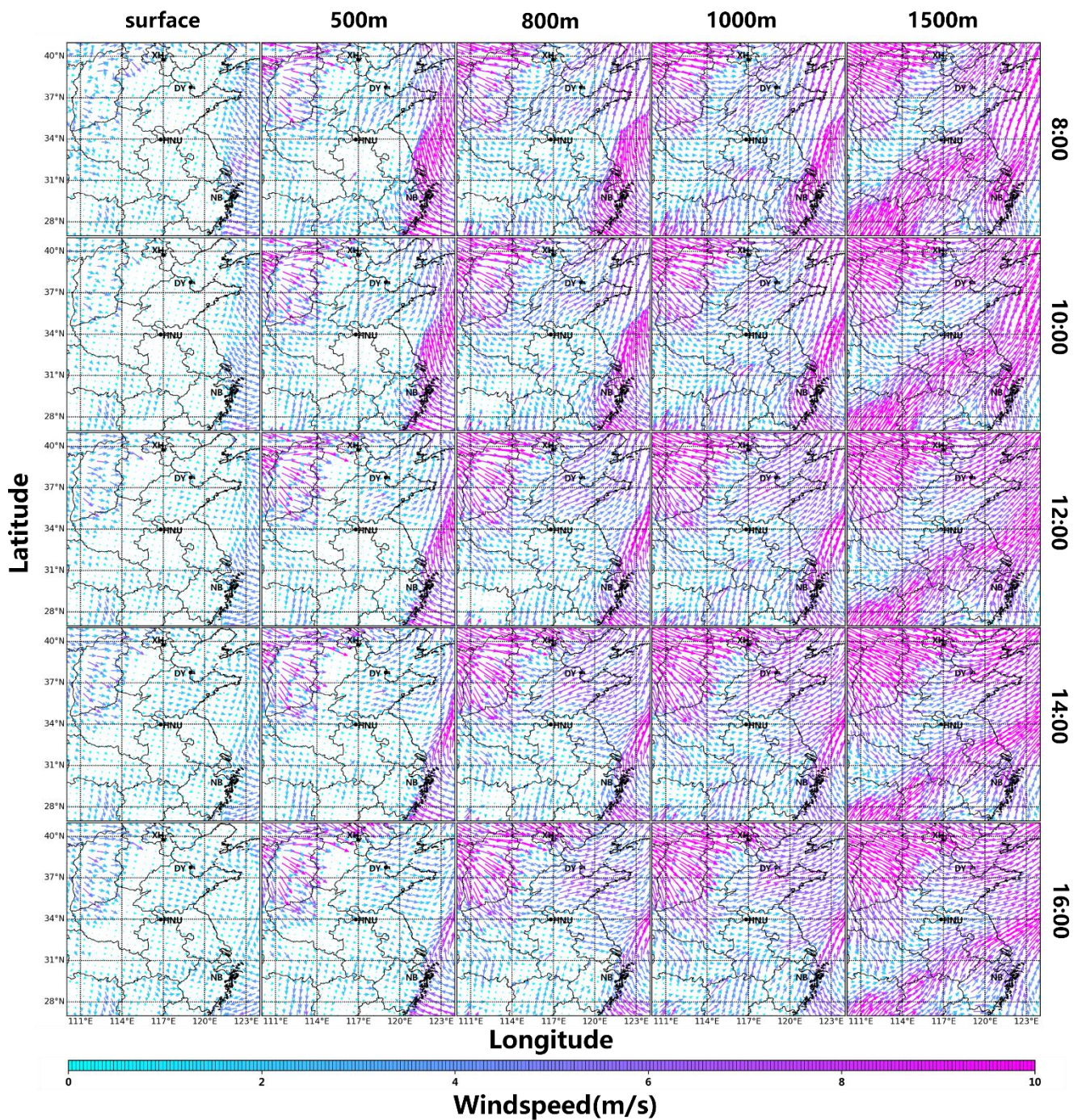


Fig. S20. The diurnal variation in wind fields in layers of surface, 500, 800, 1000 and 1500 m on **January 21, 2021**, respectively. The arrows represent the wind direction, and their lengths and colours stand for the wind speed.

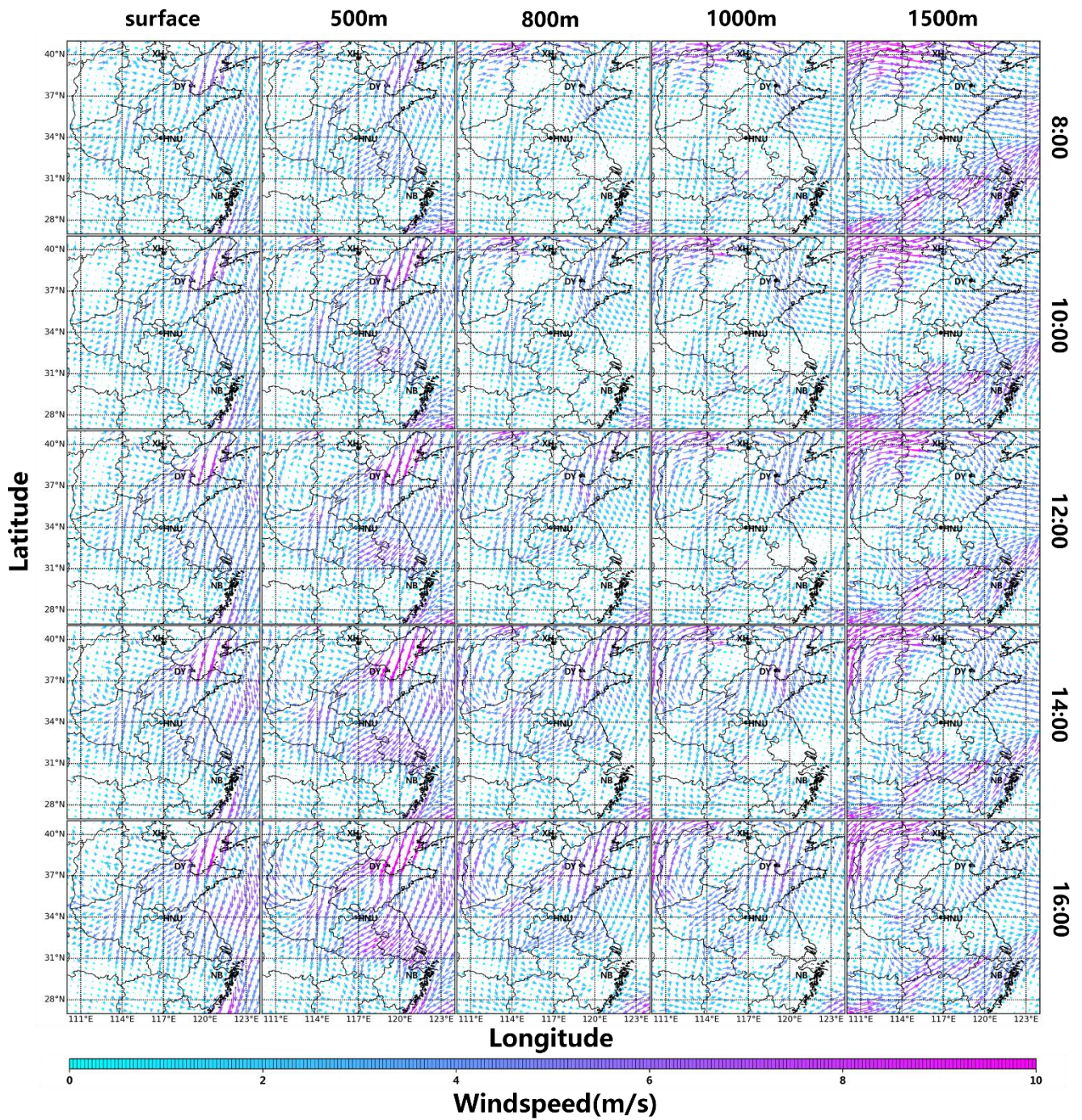


Fig. S21. The diurnal variation in wind fields in layers of surface, 500, 800, 1000 and 1500 m on **January 22, 2021**, respectively. The arrows represent the wind direction, and their lengths and colours stand for the wind speed.

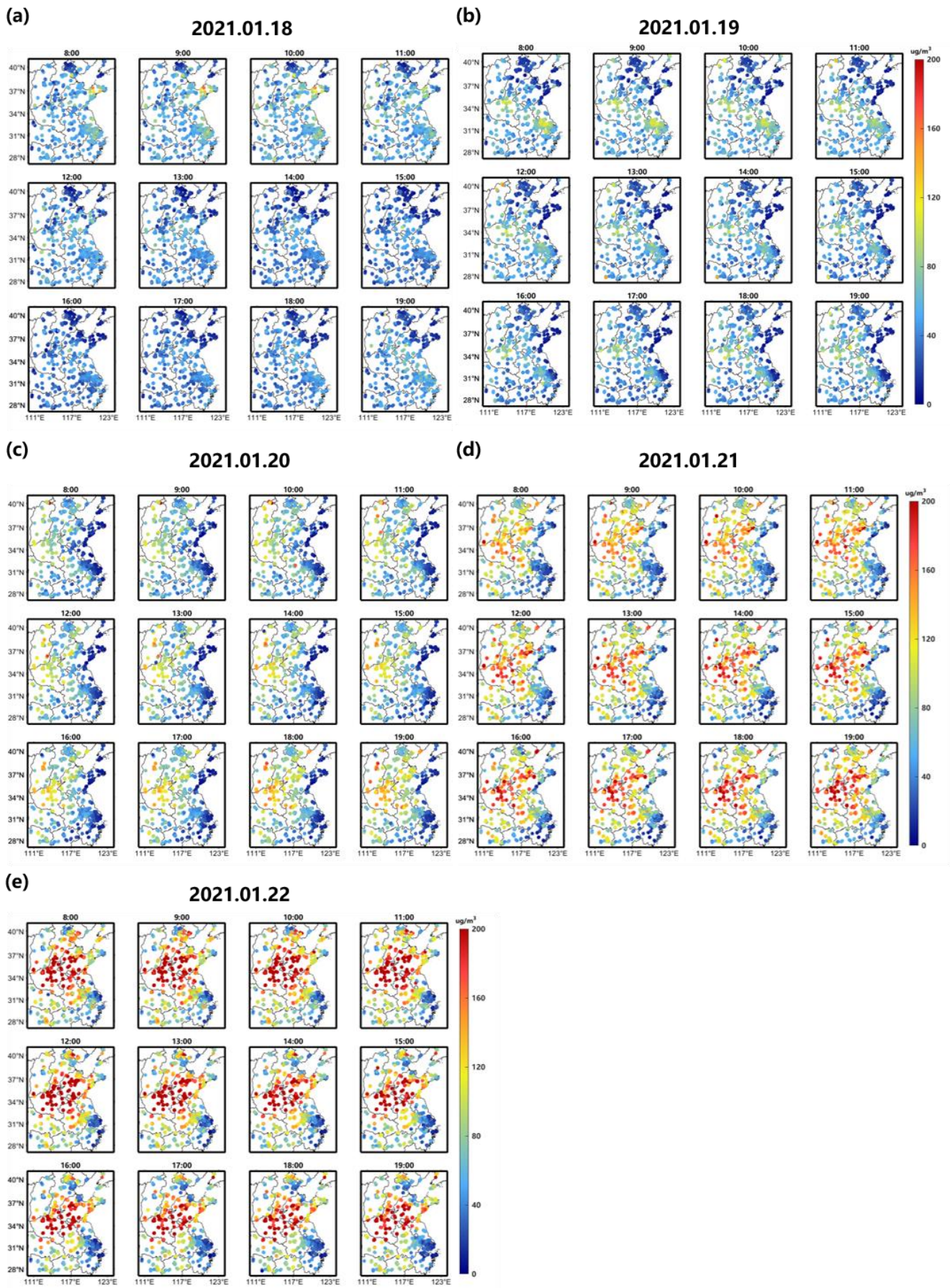


Fig. S22. The spatial distribution of PM_{2.5} concentrations collected from CNEMCs on January 18-22, 2021.

References

- Altshuller, A. P.: Production of aldehydes as primary emissions and from secondary atmospheric reactions of alkenes and alkanes during the night and early morning hours, *Atmos Environ*, 27, 21-32, 10.1016/0960-1686(93)90067-9, 1993.
- Andreae, M. O.: Emission of trace gases and aerosols from biomass burning – an updated assessment, *Atmospheric Chemistry and Physics*, 19, 8523-8546, 10.5194/acp-19-8523-2019, 2019.
- Berberan-Santos, M. N., Bodunov, E. N., and Pogliani, L.: On the barometric formula, *American Journal of Physics*, 65, 404-412, 10.1119/1.18555, 1997.
- Carrier, P., Hannachi, H., and Mouvier, G.: The Chemistry of Carbonyl-Compounds in the Atmosphere - a Review, *Atmos Environ*, 20, 2079-2099, Doi 10.1016/0004-6981(86)90304-5, 1986.
- Carvalho, D., Rocha, A., Gómez-Gesteira, M., and Santos, C.: A sensitivity study of the WRF model in wind simulation for an area of high wind energy, *Environmental Modelling & Software*, 33, 23-34, 10.1016/j.envsoft.2012.01.019, 2012.
- Chan, K. L., Wang, Z., Ding, A., Heue, K.-P., Shen, Y., Wang, J., Zhang, F., Shi, Y., Hao, N., and Wenig, M.: MAX-DOAS measurements of tropospheric NO₂ and HCHO in Nanjing and a comparison to ozone monitoring instrument observations, *Atmospheric Chemistry and Physics*, 19, 10051-10071, 10.5194/acp-19-10051-2019, 2019.
- Cleveland, W. S.: LOWESS: A Program for Smoothing Scatterplots by Robust Locally Weighted Regression *The American Statistician*, 35, 54, 10.2307/2683591 1981.
- Dong, D., Shao, M., Li, Y., Lu, S., Wang, Y., Ji, Z., and Tang, D.: Carbonyl emissions from heavy-duty diesel vehicle exhaust in China and the contribution to ozone formation potential, *Journal of Environmental Sciences*, 26, 122-128, 10.1016/s1001-0742(13)60387-3, 2014.
- Draxler, R. R. and Hess, G.: An overview of the HYSPLIT_4 modelling system for trajectories, *Aust. Meteorol. Mag.*, 47, 295-308, 1998.
- Duan, J., Tan, J., Yang, L., Wu, S., and Hao, J.: Concentration, sources and ozone formation potential of volatile organic compounds (VOCs) during ozone episode in Beijing, *Atmospheric Research*, 88, 25-35, 10.1016/j.atmosres.2007.09.004, 2008.
- Ek, M. B., Mitchell, K. E., Lin, Y., Rogers, E., Grunmann, P., Koren, V., Gayno, G., and Tarpley, J. D.: Implementation of Noah land surface model advances in the National Centers for Environmental Prediction operational mesoscale Eta model, *Journal of Geophysical Research: Atmospheres*, 108, 10.1029/2002jd003296, 2003.
- Friedfeld, S., Fraser, M., Ensor, K., Tribble, S., Rehle, D., Leleux, D., and Tittel, F.: Statistical analysis of primary and secondary atmospheric formaldehyde, *Atmos Environ*, 36, 4767-4775, 10.1016/S1352-2310(02)00558-7, 2002.
- Friedrich, M. M., Rivera, C., Stremme, W., Ojeda, Z., Arellano, J., Bezanilla, A., García-Reynoso, J. A., and Grutter, M.: NO₂ vertical profiles and column densities from MAX-DOAS measurements in Mexico City, *Atmospheric Measurement Techniques*, 12, 2545-2565, 10.5194/amt-12-2545-2019, 2019.
- Frieß, U., Monks, P. S., Remedios, J. J., Rozanov, A., Sinreich, R., Wagner, T., and Platt, U.: MAX-DOAS O₄ measurements: A new technique to derive information on atmospheric aerosols: 2. Modeling studies, *Journal of Geophysical Research*, 111, 10.1029/2005jd006618, 2006.
- Garcia, A. R., Volkamer, R., Molina, L. T., Molina, M. J., Samuelson, J., Mellqvist, J., Galle, B., Herndon, S. C., and Kolb, C. E.: Separation of emitted and photochemical formaldehyde in Mexico City using a statistical analysis and a new pair of gas-phase tracers, *Atmospheric Chemistry and Physics*, 6, 4545-4557, 10.5194/acp-6-4545-2006, 2006.
- García-Bustamante, E., Jiménez, P. A., González-Rouco, J. F., Valero, F., Montávez, J. P., and Navarro, J.: Surface Wind Regionalization in Complex Terrain, *Journal of Applied Meteorology and Climatology*, 47, 308-325, 10.1175/2007jamc1483.1, 2008.
- Grell, G. A. and Dévényi, D.: A generalized approach to parameterizing convection combining ensemble and data assimilation techniques, *Geophysical Research Letters*, 29, 38-31-38-34, 10.1029/2002gl015311, 2002.
- Greenblatt, G. D., Orlando, J. J., Burkholder, J. B., and Ravishankara, A. R.: Absorption measurements of oxygen between 330 and 1140 nm, *Journal of Geophysical Research*, 95, 18577-18582, 10.1029/JD095iD11p18577, 1990.

Hong, Q., Liu, C., Chan, K. L., Hu, Q., Xie, Z., Liu, H., Si, F., and Liu, J.: Ship-based MAX-DOAS measurements of tropospheric NO₂, SO₂, and HCHO distribution along the Yangtze River, *Atmospheric Chemistry and Physics*, 18, 5931-5951, 10.5194/acp-18-5931-2018, 2018.

Hong, Q., Liu, C., Hu, Q., Xing, C., Tan, W., Liu, H., Huang, Y., Zhu, Y., Zhang, J., Geng, T., and Liu, J.: Evolution of the vertical structure of air pollutants during winter heavy pollution episodes: The role of regional transport and potential sources, *Atmospheric Research*, 228, 206-222, 10.1016/j.atmosres.2019.05.016, 2019.

Lee, M., Heikes, B. G., Jacob, D. J., Sachse, G., and Anderson, B.: Hydrogen peroxide, organic hydroperoxide, and formaldehyde as primary pollutants from biomass burning, *Journal of Geophysical Research: Atmospheres*, 102, 1301-1309, 10.1029/96jd01709, 1997.

Levy, H.: Normal Atmosphere: Large Radical and Formaldehyde Concentrations Predicted, *Science*, 173, 141-143, 10.1126/science.173.3992.141, 1971.

Lin, Y. L., Farley, R. D., and Orville, H. D.: Bulk parameterization of the snow field in a cloud model, *Journal of Applied Meteorology*, 22, 1065-1092, 10.1175/1520-0450(1983)022<1065:BPOTSF>2.0.CO;2, 1983.

Liu, C., Zhang, C., Mu, Y., Liu, J., and Zhang, Y.: Emission of volatile organic compounds from domestic coal stove with the actual alternation of flaming and smoldering combustion processes, *Environ Pollut*, 221, 385-391, 10.1016/j.envpol.2016.11.089, 2017.

Liu, H., Liu, C., Xie, Z., Li, Y., Huang, X., Wang, S., Xu, J., and Xie, P.: A paradox for air pollution controlling in China revealed by "APEC Blue" and "Parade Blue", *Sci Rep*, 6, 34408, 10.1038/srep34408, 2016.

Mlawer, E. J., Taubman, S. J., Brown, P. D., Iacono, M. J., and Clough, S. A.: Radiative transfer for inhomogeneous atmospheres: RRTM, a validated correlated-k model for the longwave, *Journal of Geophysical Research: Atmospheres*, 102, 16663-16682, 10.1029/97jd00237, 1997.

Orrell, D., Smith, L., Barkmeijer, J., and Palmer, T. N.: Model error in weather forecasting, *Nonlinear Processes in Geophysics*, 8, 357-371, 10.5194/npg-8-357-2001, 2001.

Ou, J., Hu, Q., Liu, H., Hong, Q., Xing, C., Tan, W., Lin, H., Wang, X., Xu, H., Zhu, P., and Liu, W.: Vertical characterization and potential sources of aerosols in different seasons over the Yangtze River Delta using ground-based MAX-DOAS, *Environ Pollut*, 279, 116898, 10.1016/j.envpol.2021.116898, 2021.

Rodgers, C. D., Taylor, F. W. (Ed.): *Inverse methods for atmospheric sounding, theory and practice*, World Scientific, 255 pp.2004.

Shimada, S., Ohsawa, T., Chikaoka, S., and Kozai, K.: Accuracy of the Wind Speed Profile in the Lower PBL as Simulated by the WRF Model, *Sola*, 7, 109-112, 10.2151/sola.2011-028, 2011.

Su, W., Liu, C., Hu, Q., Zhao, S., Sun, Y., Wang, W., Zhu, Y., Liu, J., and Kim, J.: Primary and secondary sources of ambient formaldehyde in the Yangtze River Delta based on Ozone Mapping and Profiler Suite (OMPS) observations, *Atmospheric Chemistry and Physics*, 19, 6717-6736, 10.5194/acp-19-6717-2019, 2019.

Wagner, T., Dix, B., Friedeburg, C. v., Frieß, U., Sanghavi, S., Sinreich, R., and Platt, U.: MAX-DOAS O₄ measurements: A new technique to derive information on atmospheric aerosols-Principles and information content, *Journal of Geophysical Research*, 109, n/a-n/a, 10.1029/2004jd004904, 2004.

Wang, Y., Lampel, J., Xie, P., Beirle, S., Li, A., Wu, D., and Wagner, T.: Ground-based MAX-DOAS observations of tropospheric aerosols, NO₂, SO₂ and HCHO in Wuxi, China, from 2011 to 2014, *Atmospheric Chemistry and Physics*, 17, 2189-2215, 10.5194/acp-17-2189-2017, 2017.

Wang, Z., Liu, C., Xie, Z., Hu, Q., Andreae, M. O., Dong, Y., Zhao, C., Liu, T., Zhu, Y., Liu, H., Xing, C., Tan, W., Ji, X., Lin, J., and Liu, J.: Elevated dust layers inhibit dissipation of heavy anthropogenic surface air pollution, *Atmospheric Chemistry and Physics*, 20, 14917-14932, 10.5194/acp-20-14917-2020, 2020.

Wood, E. C., Canagaratna, M. R., Herndon, S. C., Onasch, T. B., Kolb, C. E., Worsnop, D. R., Kroll, J. H., Knighton, W. B., Seila, R., Zavala, M., Molina, L. T., DeCarlo, P. F., Jimenez, J. L., Weinheimer, A. J., Knapp, D. J., Jobson, B. T., Stutz, J., Kuster, W. C., and Williams, E. J.: Investigation of the correlation between odd oxygen and secondary organic aerosol in Mexico City and Houston, *Atmospheric Chemistry and Physics*, 10, 8947-8968, 10.5194/acp-10-8947-2010, 2010.

Xue, J., Zhao, T., Luo, Y., Miao, C., Su, P., Liu, F., Zhang, G., Qin, S., Song, Y., Bu, N., and Xing, C.: Identification of ozone sensitivity for NO₂ and secondary HCHO based on MAX-DOAS measurements in northeast China, *Environ Int*, 160, 107048, 10.1016/j.envint.2021.107048, 2022.